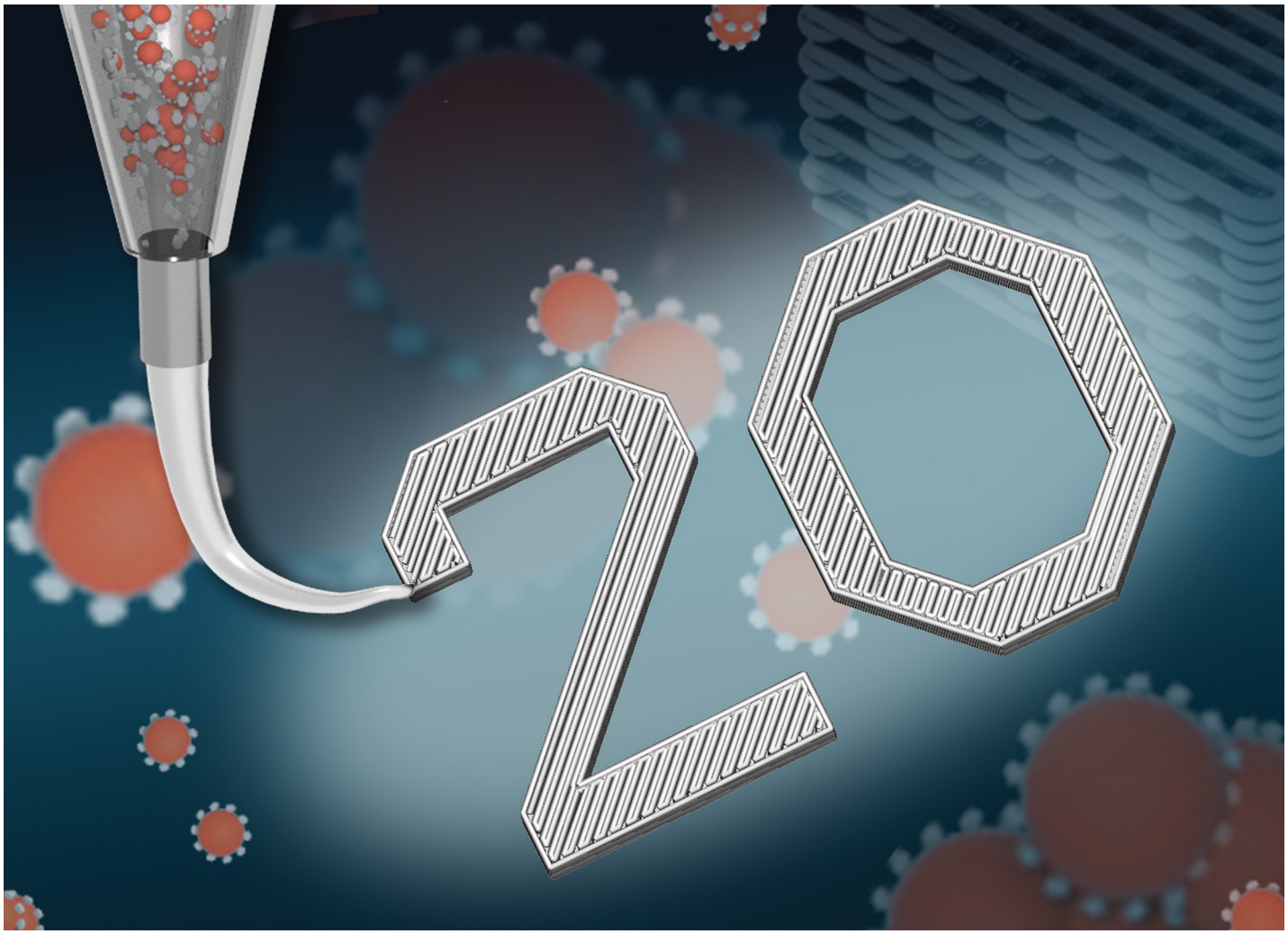

Showcasing research from Dr Esther García-Tuñón's laboratory, School of Engineering and Materials Innovation Factory, University of Liverpool, Liverpool, UK.

Designing yield stress fluids for advanced materials processing using derivatives of pH-responsive branched co-polymer surfactants

Bringing together polymer chemistry, advanced materials, complex fluids and rheology, this paper demonstrates the importance of the structure–properties relationship of emulsified suspensions stabilised by pH-responsive branched copolymer surfactants (BCSs). Their distinctive nonlinear behaviours during yielding correlate with the printing behaviour and shape fidelity. Exploiting BCS electro-steric stabilisation enables the formulation of stable strontium titanate emulsion gels to fabricate hierarchical structures *via* direct ink writing. Porosity can be tuned at multiple levels from mm patterned structures to micron-sized porous filaments.

Image reproduced by permission of Esther García-Tuñón from *Soft Matter*, 2025, **21**, 4822.

The authors acknowledge Xingyue Zhang, Zhidong Leo and Esther García-Tuñón for their contributions to the artwork.

As featured in:

See Esther García-Tuñón *et al.*, *Soft Matter*, 2025, **21**, 4822.

ROYAL SOCIETY OF CHEMISTRY

rsc.li/soft-matter-journal

Registered charity number: 207890

Soft Matter

PAPER

View Article Online
View Journal | View Issue

Cite this: *Soft Matter*, 2025, **21**, 4822

Designing yield stress fluids for advanced materials processing using derivatives of pH-responsive branched co-polymer surfactants†

Emma L. Jones, [ab] Zhidong Luo,[b] Rishav Agrawal,[b] Sean Flynn,[b] Megan Carr,[c] Will Sharratt [b] and Esther García-Tuñón *[bc]

Through careful formulation design from a structure–properties perspective, this work demonstrates the potential of pH-responsive branched co-polymer surfactants (BCSs) in emulsion engineering and advanced materials processing. A library of BCS derivatives, with controlled spatial distribution of hydrogen bonding motifs and different branching levels, is synthesised *via* a modified Strathclyde method with varying conditions in solids content and PEGMA chain length. High dilution during the co-polymerisation leads to linear co-polymers, while an increase of monomers concentration favours branching reactions. This diverse set of BCSs can be exploited to stabilise pH-responsive suspension and emulsions containing activated charcoal (AC) or strontium titanate (STO) to create an array of yield stress soft materials. Large amplitude oscillatory shear (LAOS) experiments reveal their diverse rheological properties and yielding behaviours, that correlate primarily with powders properties and concentration, the degree of branching of BCS macromolecules, and to some extent, with the PEGMA length or BCS molecular weight. Based on the rheological characterisation, two formulations are selected and optimised for direct coagulation casting of AC suspensions and direct ink writing (DIW) of STO to create macroscopic structures. The optimised STO emulsion gels for DIW show a dramatic shift in printing behaviour before and after triggering the pH-controlled assembly. LAOS analyses using Fourier-transform (FT) rheology and the sequence of physical processes (SPP) confirm that the pH triggered assembly of STO emulsion gels results in the transition from a stable microstructure that shows a smooth flow transition, to an aggregated and unstable microstructure that becomes easily disrupted under shear. The higher harmonics and SPP analysis enable the correlation of yielding and printing behaviours. Overall, the findings highlight the critical role that BCSs play in providing electro-steric stabilisation of suspensions and emulsion gels in the processing of advanced materials. Combining polymer chemistry, formulation design and rheology, we optimise responsive formulations to create complex macroscopic structures with hierarchical features.

Received 11th December 2024,
Accepted 15th April 2025

DOI: 10.1039/d4sm01473a

rsc.li/soft-matter-journal

1 Introduction

Developing reliable and tunable processing strategies is key to expand the range of advanced materials (*e.g.* ceramics,[1,2] 2D materials,[3,4] perovskites,[5] and porous organic cages[6] to name a few) that can be used in engineering solutions to issues such as the climate crisis and the rollout of alternative renewable energy sources. The ability to process these materials while preserving their functional properties is crucial to their application.[1] The choice of additives (*e.g.* surfactants, rheology modifiers, dispersants, flocculants and curing agents) incorporated in formulations to aid processing should not limit nor damage the functional performance. An ideal formulation is simple, non-toxic (water-based) and with a minimal amount of additives to achieve the required rheology and processability. This is of particular importance in the processing of materials that must undergo drying and sintering post-processing steps without compromising their properties due to binders removal.[7,8]

Surfactants are key additives in formulations, where their amphiphilic nature enables a "plethora" of solution-processed applications through the stabilisation of hydrophobic nanomaterials in water.[7–10] Surfactants with chemical moieties able to undergo reversible changes in response to external stimuli are

[a] *The Leverhulme Research Centre for Functional Materials Design, UK*
[b] *School of Engineering, University of Liverpool, UK.*
E-mail: egarciat@liverpool.ac.uk
[c] *Materials Innovation Factory, University of Liverpool, UK*

† Electronic supplementary information (ESI) available: Additional figures and methodologies included in a pdf file. See DOI: https://doi.org/10.1039/d4sm01473a

particularly promising to precisely control both interfacial and bulk solution behaviours.[11–13] These surfactants enable formulation of "smart" systems such as emulsions[14,15] nanoparticles[12] and emulsified suspensions[10,16] that aid the facile processing of advanced materials through the design of complex fluids with tunable rheology.[17–19] In these systems, triggering a change in the surfactant structure, conformation or charge by modifying the pH, ionic strength or exposing to light, for example, can lead to significant yet reversible changes in formulation properties.

Branched co-polymer surfactants (BCSs), a class of stimuli-responsive macromolecular amphiphiles,[14,15,20] have been previously investigated for their use as drug delivery systems, facilitated by their pH-mediated switchable behaviour. BCSs are synthesised through free radical polymerisation (Strathclyde methodology) of poly(ethylene glycol)methacrylate (PEGMA), methacrylic acid (MAA) and ethylene glycol dimethacrylate (EGDMA) primary chains capped with hydrophobic DDT chain ends.[20] These BCSs undergo on-demand pH-triggered destabilisation of oil-in-water emulsions,[14] or assembly into structured, gel-like soft solids.[15] This responsive behaviour has been shown to be driven by a more complex process involving polymer restructuring, and at least two types of inter-polymer interactions.[21]

Owing to their controlled aggregation, BCSs have been exploited as multi-functional additives (*e.g.* stabilising, binding and as rheology modifiers) for ceramics and graphene based materials.[10,16,17] At high pH, BCS provides electro-steric stabilisation of ceramic particles (and other materials) in water that show nearly Newtonian or slightly viscoelastic behaviour. When triggering the assembly through a pH-switch below the pK_a, particles and/or droplets form a physical gel with elasto-visco-plastic behaviours.[16] The responsive behaviour of BCSs can be exploited to design complex (yield stress) fluids[19] for advanced materials fabrication methods, for example in casting and direct ink writing (DIW). DIW requires careful design and understanding of soft materials with specific rheological properties and yielding behaviours.[22,23]

Here we first produce and examine a library of BCS derivatives (BCS_{dev}) using modifications to the original BCS Strathclyde methodology by carrying out co-polymerisations of PEGMA macromonomers with different chain lengths and dilution conditions (from 10 to 50 wt% solids, Section 3.1). The subtle differences in co-polymer composition and topology are then exploited to formulate two materials as model systems, activated charcoal (AC) and strontium titanate (STO). AC is studied as the "stretch" material based on its limited water-processability. STO is chosen as a model ceramic oxide with functional properties in photo-catalytic applications.

Using BCS derivatives to stabilise and control the aggregation of AC suspensions and STO emulsions, we systematically investigate the properties of the resultant library of yield stress fluids using oscillatory rheology (Section 3.2). The results from this "scouting" study using large amplitude oscillatory shear (LAOS)[24] inform the selection of two final formulations with potential for casting (AC, Section 3.3.1) and DIW (STO, Section 3.3.2).

Using transient data collection, complementary mathematical frameworks (Fourier-transform rheology,[25,26] and the sequence of physical processes, SPP[27–29]) this work provides a quantitative comparison of STO formulations' non-linearities, yielding processes and flow instabilities before and after aggregation driven by the pH-responsive behaviour. The elastic Lissajous–Bowditch plots, G', G'', $\frac{I_3}{I_1}$ and the dissipation ratio (ϕ)[30] show distinctive trends that correlate with printing resolution.[23]

Bringing together polymer chemistry, formulation design, complex fluids and rheology, this work provides a multi-disciplinary approach to design DIW ceramic feedstocks, and to study the underlying structure–rheology relationship that impact the shape fidelity that can be achieved during the DIW process. These findings open up new opportunities to fabricate hierarchical structures using functional materials.

2 Materials and methodologies

2.1 Reagents and materials

Poly(ethylene glycol)methyl ether methacrylate (PEGMA, average M_n 950 g mol^{-1}, 500 g mol^{-1} or 350 g mol^{-1}), methacrylic acid (MAA), ethylene glycol dimethacrylate (EGDMA), 1-dodedanethiol (DDT), tetramethylsilane (TMS), glucono-δ-lactone (GdL), dodecane, deuterated methanol (MeOD), and sodium nitrate ($NaNO_3$) were purchased from Sigma Aldrich and used as received. Azobis(isobutyronitrile) (AIBN) was purchased from Sigma Aldrich and recrystalised from methanol (MeOH) prior to use. Activated charcoal (AC) powders were purchased from Sigma Aldrich and milled with ceramic milling balls for 24 hours prior to use. Strontium titanate ($SrTiO_3$; STO) micropowders were purchased from Alfa Aesar and milled with ceramic milling balls for 24 hours prior to use. Ethanol (EtOH), methanol and petroleum ether, purchased from Fischer Scientific, were of standard laboratory grade. Sodium hydroxide (NaOH) and 37% hydrochloric acid (HCl) were purchased from Fisher Scientific and diluted in deionised H_2O to produce 0.1 M and 1.0 M stock solutions of each. Pluronic® F-127 was purchased from Sigma Aldrich and dissolved in distilled H_2O to yield a 25 wt% stock solution. This stock was stored in a refrigerator at ≈4 °C.

2.2 Analytical techniques

^{1}H nuclear magnetic resonance (NMR) spectra of the BCSs synthesised in this work were recorded in MeOD using a Bruker Avance spectrometer operating at 400 MHz. Chemical shifts (δ) are reported in parts per million (ppm) and TMS was used as an internal standard for ^{1}H NMR spectra. All NMR spectra were analysed using TopSpin 3 (Bruker, licensed to the University of Liverpool).

Triple detection size exclusion chromatography (TD-SEC) was performed using a Malvern OMNISEC resolve/reveal system equipped with refractive index, viscometry and dual-angle light scattering detectors; a mobile phase of water, MeOH (20 v/v%), sodium nitrate (0.05 M) and NaOH (0.004 M) were employed with a flow rate of 0.8 mL min^{-1}; two Viscotek GMPWXL columns and an additional guard column were used with an oven temperature of 40 °C to determine the molar mass, molar mass distribution and Mark–Houwink α values. Aqueous

pullulan and dextran solutions were used for universal calibration. The results for each co-polymer are given as an average with errors given as standard deviation from the mean.

pH measurements were taken with a SevenCompact S220 pH/Ion meter with InLab Expert Pro-ISM probe, calibrated daily using pH 4, 7 and 10 buffer solutions.

2.3 Synthesis of "original" BCS

The following procedure describes a typical synthesis of a branched co-polymer surfactant (BCS, that corresponds to sample L1 in this work) targeting a 1 : 1 stoichiometric molar ratio of methacrylic acid (MAA) to ethylene glycol (EG) units as described by Woodward *et al.* using the Strathclyde methodology, DDT-p(PEGMA$_{0.5}$-*co*-MAA$_{9.5}$-*co*-EGDMA$_{1.0}$).[14] PEGMA (M_n = 950 g mol^{-1}, 0.500 g, 0.53 mmol, 0.5 eq.), MAA (0.861 g, 10.00 mmol, 9.5 eq.), EGDMA (0.209 g, 1.05 mmol, 1.0 eq.), DDT (0.213 g, 1.05 mmol, 1.0 eq.), AIBN (0.009 g, 0.05 mmol, 0.5 eq.) and ethanol (EtOH, 16.121 g, 90 wt% w.r.t. total mass) were added to an oven dried round bottomed flask. The flask was sealed and purged with N_2 for 30 minutes before the addition of TMS (0.2 mL, stored under N_2). The flask was heated to 70 °C and stirred for 48 hours. The reaction was quenched by rapid cooling to 0 °C in an ice bath. Aliquots (*ca.* 100 μL) prior to and post reaction (t_0 and t_f, respectively) were taken for ^{1}H NMR analysis. The solution was dried *in vacuo* before redissolution in minimal EtOH and precipitated into cold petroleum ether twice to yield a viscous, opaque oil. The polymer was dried *in vacuo* at 40 °C for 24 hours and characterised *via* ^{1}H NMR and TD-SEC. Syntheses were completed in triplicate to verify the reliability before larger scale syntheses were performed for complex fluid formulation.

2.4 Synthesis of BCS derivatives

A library of water-soluble BCS derivatives was synthesised *via* DDT-mediated free radical co-polymerisations of MAA, PEGMA and EGDMA using slight modifications to the method described in Section 2.3.[20] Initial polymer syntheses (S1, M1 and L1, Table 1) varied PEGMA chain lengths (number average molecular weights M_n, of 300, 500 and 950 g mol^{-1}) and therefore in comonomer distributions within BCS primary chains, whilst limiting chain branching at high-dilution in line with previously reported BCS syntheses.[14,15] BCS co-polymerisations were conducted using comparable initial molar ratios of the bifunctional comonomer, EGDMA, to chain transfer agent, DDT ($[EGDMA]_0/[DDT]_0$ = 0.90–1.09). To achieve an equimolar ratio of hydrogen bond donor and acceptor units,[15] all polymer syntheses targeted equimolar ratios of MAA and PEG repeat units in the resulting BCS; this required targeting initial MAA to PEGMA molar ratios $\frac{[PEGMA]_0}{[PEGMA]_0+[MAA]_0}$ in Table 1 when using PEGMA macromonomers with M_n values of 950, 500 and 300 g mol^{-1} respectively. Conversion and concentration ratios were determined from ^{1}H NMR as explained in the ESI† (Fig. S1 and S2).

2.5 Powders characterisation

Particle sizing was conducted on a Malvern Mastersizer 3000 fitted with a HydroMV dispersion unit *via* static laser light scattering. Sizes were calculated as the average of 3 samples, each with 10 measurements taken, with errors given as the standard deviation from the mean.

Water contact angle (WCA) determination was performed using a Kruss DSA100E Dynamic Shape Analyser from sessile droplets at room temperature on an 8 mm pellet formed from dry material. The baseline was fitted manually, and the angle determined using a Young–Laplace fitting method. For BCS-stabilised samples, glass slides were coated in a small amount of each suspension and allowed to dry overnight under IR irradiation.

Brunauer–Emmett–Teller (BET). Surface area isotherms were generated in triplicate using a Micromeritic 3-Flex 3500 multi-port high throughput gas adsorption analyser. Errors are given as the standard deviation from the mean.

Scanning electron microscopy (SEM) imaging was performed on a Hitachi S-4800 SEM. Samples were mounted on aluminium SEM stubs using a carbon tape and edges painted with PELCO conductive silver paint. These samples were subsequently coated with chromium in a Q150T Plus sputter coater for 90 seconds.

Results for activated charcoal (AC, Fig. S4 and S5, ESI†) and strontium titanate (STO, Fig. S6 and S7) are included in the ESI.†

2.6 Formulation process

BCS powders for each BCS derivative were dispersed in distilled water using NaOH 1 M to adjust the pH to 7.5 until a transparent, homogeneous stock solution was obtained.

Table 1 ^{1}H NMR results for BCSs derivatives synthesised in this work

Polymer			^{1}H NMR (MeOD)			
BCS_{dev}	Mon. conc. (wt%)	Formula	$\frac{[PEGMA]_0+[MAA]_0+[EGDMA]_0}{[DDT]_0}$	$\frac{[EGDMA]_0}{[DDT]_0}$	$\frac{[PEGMA]_0}{[PEGMA]_0+[MAA]_0}$	Conversion (%)
L1	10	DDT-P(PEGMA$_{0.5}$-*co*-MAA$_{8.4}$-EGDMA$_{1.1}$)	11.4	0.90	0.056	83.1
L3	30	DDT-P(PEGMA$_{0.5}$-*co*-MAA$_{8.8}$-EGDMA$_{1.0}$)	12.3	0.94	0.054	99.7
L5	50	DDT-P(PEGMA$_{0.5}$-*co*-MAA$_{8.4}$-EGDMA$_{0.9}$)	11.8	0.83	0.056	99.9
M1	10	DDT-P(PEGMA$_{1.0}$-*co*-MAA$_{8.3}$-EGDMA$_{1.0}$)	14.0	1.09	0.108	91.7
M3	30	DDT-P(PEGMA$_{1.0}$-*co*-MAA$_{7.4}$-EGDMA$_{0.9}$)	12.1	0.96	0.118	97.7
M5	50	DDT-P(PEGMA$_{1.0}$-*co*-MAA$_{7.7}$-EGDMA$_{0.7}$)	12.0	0.82	0.114	99.4
S1	10	DDT-P(PEGMA$_{2.0}$-*co*-MAA$_{6.8}$-EGDMA$_{1.0}$)	12.3	1.05	0.226	99.8
S3	30	DDT-P(PEGMA$_{2.0}$-*co*-MAA$_{7.0}$-EGDMA$_{1.0}$)	11.2	0.96	0.223	100
S5	50	DDT-P(PEGMA$_{2.0}$-*co*-MAA$_{7.4}$-EGDMA$_{0.8}$)	11.4	0.81	0.213	100

Stock solutions for the ''scouting'' study in Section 3.2 contained 1.2 wt% BCS w.r.t. the stock solution volume. STO optimised formulations for DIW were prepared with a 2 wt% BCS stock solution. These were subsequently used as a base to prepare a library of formulations containing activated charcoal (AC) or strontium titanate ($SrTiO_3$, STO). Each powdered material (AC and STO) was fully characterised both pre and post-milling to ensure that there was no significant differences in the chemistry, structure, or purity as a result of the milling process (Fig. S4–S7, ESI†). The details for each formulation and corresponding rheological metrics are included in Table 3.

2.6.1 BCS-stabilised suspensions. BCS stock was used to disperse the powders *via* ball milling to facilitate electro-steric stabilisation.[10,16] After a preliminary study the solids amounts were fixed at the maximum concentrations that could be dispersed (Table 3). AC suspensions were prepared by dispersing 12 vol% of AC powders in BCS stock solution (1.2 wt% w.r.t. to stock solution volume). These suspensions are labelled as 12-AC through the manuscript. STO formulations were prepared with a fixed concentration of 47 vol%, labelled as 47-STO. Formulations were milled for up to 24 hours on a TURBULA T2F Shaker-Mixer after the addition of ceramic milling media (where the mass of alumina balls added comprised 1/3rd of the total mass of the particles and container).

2.6.2 BCS-stabilised emulsions. STO BCS-stabilised emulsions were prepared using an IKA T-18 digital ULTRA-TURRAX® disperser fitted with a S18N-10G dispersion tool. Emulsions were prepared with BCS-STO : decane volume rations of 60 : 40. Emulsification conditions were fixed at 24 000 rpm for 2 min.

AC suspensions could not be emulsified to produce stable formulations. This is likely due to the presence of large particles with irregular shapes. AC suspensions were directly assembled (without the emulsification step) to study their rheology and shaping ability (Sections 4 and 5 respectively).

2.6.3 Triggered assembly of BCS formulations. AC suspensions and STO emulsions were assembled into gels through the activation of multiple hydrogen bonds between MAA and PEGMA branches. GδL (with concentrations between 2 and 8 wt% w.r.t. total volume) or HCl solutions (1 M) were added to AC and STO formulations to trigger the assembly of particle and/or droplets.[10,16] Each gel was then stored in a sealed container under ambient conditions for a minimum of 24 hours prior to rheological analysis.

2.7 Rheological measurements

A strain controlled rheometer ARES G2 (TA Instruments) has been used for all the rheological measurements with slightly different settings for the ''scouting'' study in Section 3.2, and the advanced characterisation performed on selected DIW formulations in Section 3.4.

In large amplitude oscillatory shear (LAOS) measurements, an oscillatory input strain is applied on the material, and the resultant output stress is measured for every prescribed strain amplitude. A wide range of strain amplitude values (γ_0, between 0.01% and 500%) enable us to investigate the structure deformation from small amplitude oscillatory shear (SAOS) to LAOS.[24] The ARES G2 rheometer and the TRIOS software allow to collect the strain amplitude sweep data in either correlation mode or transient mode. The former provides the first-harmonic moduli, G', G'' and the latter provides the raw strain/stress waveforms.

Preliminary LAOS tests were performed for all formulations (Table 3) to study the behaviour of each BCS derivative within our library and to compare the resultant properties of each formulation. These ''scouting'' LAOS tests were performed using the correlation data collection option in the TRIOS software and a 40 mm cross hatched/stainless steel serrated upper parallel plate fitted with a solvent trap. Water was placed at the top of the geometry within the rim to ensure that drying was minimised during the data collection. An exponential closure profile was set to minimise altering the structure of the sample prior measurement. The gap was set at 1 mm and the temperature fixed at 25 °C. Strain amplitude values (γ_0) ranged between 0.01% and 500%, with a fixed oscillation frequency of 0.5 Hz. The first-harmonic moduli, G', G'' are given by the TRIOS software.

STO formulations for DIW (Section 3.4) are compared using LAOS analysis on transient data (raw signals),[23] collected for 3 cycles of oscillation for every strain amplitude at a frequency of 1024 points per cycle. The measurement gap was 1 mm, using 40 mm stainless steel sandblasted parallel plates with a solvent trap. The temperature was maintained at 23 °C using a Peltier plate. Drying was prevented by placing a thin layer of low viscosity oil at the edge of the sample.

LAOS analyses are widely use to characterise yield stress fluids (*e.g.* BCSs,[20] branched polymer melts,[31] and DIW[22]). The analysis of LAOS transient data is carried out using existing mathematical frameworks: Fourier-transform (FT) rheology,[25,26] and the sequence of physical processes (SPP).[27] These complementary frameworks provide valuable insights on the underlying yielding process and its role in printing performance.[23] These mathematical frameworks are explained in more detail in the ESI† and previous publications.[23,25,27] From these analyses we determine characteristic rheological metrics for each STO formulation: storage and loss moduli (G' and G'' respectively), stress value at the onset of non-linearities (σ_{nl}) and the relative intensity of the third w.r.t. the first harmonic I_3/I_1 obtained through the FT analysis, stress overshoot or maximum stress value in the amplitude sweep (σ_{max}), stress value at the moduli crossover (flow stress, σ_f, $G' = G''$), and the dissipation ratio (ϕ,[30] eqn (S3) in ESI†). Elastic Lissajous–Bowditch (LB) curves (σ/σ_0 *vs.* γ/γ_0) are used to present the raw data. The SPP intercycle trajectories are presented in Cole–Cole plots (G_t'' *vs.* G_t') in Section 3.4.

2.8 Casting and direct ink writing (DIW)

AC suspensions (1 wt% BCS-M3 and 12 vol% AC powders w.r.t. water volume) were directly poured into moulds (coated with a thin layer of grease to facilitate de-moulding) with different shapes immediately after adding GδL (2 wt% w.r.t. total volume) to trigger particle assembly. The samples were left to dry under ambient conditions, which led to even shrinking.

Once dry, samples were easily detached from the walls and de-moulded.

STO formulations for DIW (2 wt% BCS-L5 and 47 vol% AC powders w.r.t. water volume, emulsified with NR–decane with a 60 : 40 ratio, Table 3) were prepared using sieved (raw) STO powders. DIW is carried out using a custom built robocaster[6,23] with three individual syringe plungers connected to linear actuators driven by an Aerotech A3200 machine controller using G-code. Selected STO emulsified suspensions (BCSL5-STO 47 vol% suspension emulsified with 40 vol% decane (60 : 40 ratio) at 24 000 rpm for 2 min) at different pH values (≈11 and 3 respectively) are carefully loaded into a 5 mL syringe (Nordson, EFD) with a spatula to avoid air bubbles being trapped inside. Desired 3D printed parts are designed using the software RoboCad (v5, by 3D Inks, Oklahoma) that generates the G-code for the Aerotech motion composer. The parts are printed straight onto acrylic or alumina substrates using stainless steel nozzles with a tip diameter of 0.51 mm. Printing settings were optimised for each STO formulation to achieve a continuous filament,[32] with extrusion (V_e) and motion (V_m) velocities of 1.2 and 1 mm s^{-1} respectively for the sample at pH ≈ 11, and 1.5 and 1 mm s^{-1} at pH ≈ 3. Once a printed part is completed, it is left to dry at room temperature ≈22 °C for 48 hours. The DIW set up is equipped with an *in situ*-visualisation system FLIR Blackfly S-BFS-U3-32S4M with a Nikon 35 mm f/2 wide-angle lens to record at 10 fps at 3.14 MP resolution.

2.9 Fluorescence microscopy and image analysis

47-STO BCSL5 emulsions were prepared using 40 mL decane dyed with 1 mL of ethanol-Nile red (NR) stock solution (1 mg mL^{-1}) used as fluorescent probe. Images were taken using an Olympus IX73 inverted microscope with LED fluorescence excitation light source (CL-pE300lite-DC-SB), DP75 camera and filter sets optimised for TRED (exciter: 540 to 580 nm, beam splitter: 600 nm, barrier: 620 to 650 nm).

Image analysis to determine droplet size was conducted either directly on fluorescence microscopy images, and indirectly through pore size measurement from SEM images. The latter were analysed by randomly measuring the longest inner diameters of 100 pores (reported as mean value and standard deviation in this manuscript).

3 Results and discussion

3.1 Library of BCS derivatives

Using a modified free radical polymerisation method,[14] enabled us to synthesise a library of BCS (Fig. 1) derivatives. Varying the monomer concentration (between 10 and 50 wt%) and the chain length of PEGMA macromonomers (with labels: S, M and L-series) enabled the manipulation of co-polymer composition and topology.[33] Co-polymers with a wide range of molecular weights and branched architectures (Tables 1 and 2) provide a degree of control over the properties of pH-responsive emulsions and emulsified suspensions.[20]

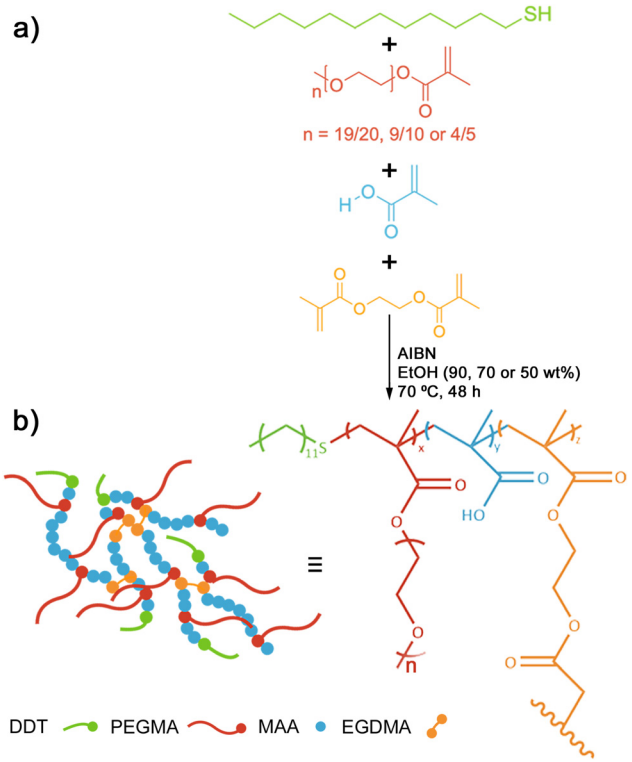

Fig. 1 (a) Free radical polymerisation scheme using a modification of the Strathclyde method to produce BCS derivatives in this work. (b) Illustrated representation of a BCS macromolecule, where DDT, PEGMA, MAA and EGDMA monomers are represented schematically and pictorially.

3.1.1 Controlling BCS comonomer distribution. FRP co-polymerisations of BCS derivatives with PEGMA macromonomers ($PEGMA_{300}$ (S), $PEGMA_{500}$ (M) and $PEGMA_{950}$ (L)) under the same conditions (10 wt% monomer concentration) as the "original" BCS[10,20] (which corresponds to L1 in this work) led to unexpected results. ^{1}H NMR analysis showed that the vinyl conversions achieved during co-polymerisations varied with the length of the PEGMA macromonomer used, with values of 83, 92 and >99% for L1, M1 and S1 respectively (Table 1). The co-polymerisations with longer PEGMA macromonomers (M1 and L1) led to vinyl conversion values below 95%, lower than any other BCSs in the literature.[20] A monomer conversion lower than 95% is associated with leftover pendant vinyl groups that have not been able to facilitate branching reactions. Triple-detection size exclusion chromatography (TD-SEC) results (Table 2, Fig. 2a) show broad monomodal molecular weight distributions, similar to those of co-polymers obtained in the absence of branching reactions.[34,35] The overlaid RI chromatograms (Fig. 2a) show comparable co-polymer molecular weight distributions regardless of vinyl conversion achieved during co-polymerisation. TD-SEC results show that co-polymerisations conducted under high dilution (S1, M1 and L1, at 10 wt% monomers concentration) produce unbranched, linear and/or cyclised BCSs (Fig. 2a and 3) with relatively low molecular weights (24 700 and 67 200 g mol^{-1} for L1 and S1 respectively, Table 2). Therefore, these co-polymers (S1, M1 and L1) may

Table 2 TD-GPC/SEC results for BCSs derivatives synthesised in this work

Polymer			TD-GPC/SEC (MeOH/H_2O)		
BCS_{dev}	Mon. conc. (wt%)	Formula	M_w (g mol^{-1})	M_n (g mol^{-1})	$Đ$
L1	10	DDT-P($PEGMA_{0.5}$-*co*-$MAA_{8.4}$-$EGDMA_{1.1}$)	24 700	12 700	1.94
L3	30	DDT-P($PEGMA_{0.5}$-*co*-$MAA_{8.8}$-$EGDMA_{1.0}$)	64 500	21 500	2.99
L5	50	DDT-P($PEGMA_{0.5}$-*co*-$MAA_{8.4}$-$EGDMA_{0.9}$)	749 000	80 500	10.96
M1	10	DDT-P($PEGMA_{1.0}$-*co*-$MAA_{8.3}$-$EGDMA_{1.0}$)	40 000	19 900	2.01
M3	30	DDT-P($PEGMA_{1.0}$-*co*-$MAA_{7.4}$-$EGDMA_{0.9}$)	169 300	36 700	4.62
M5	50	DDT-P($PEGMA_{1.0}$-*co*-$MAA_{7.7}$-$EGDMA_{0.7}$)	876 700	115 700	7.59
S1	10	DDT-P($PEGMA_{2.0}$-*co*-$MAA_{6.8}$-$EGDMA_{1.0}$)	67 200	21 400	3.16
S3	30	DDT-P($PEGMA_{2.0}$-*co*-$MAA_{7.0}$-$EGDMA_{1.0}$)	75 300	33 100	2.26
S5	50	DDT-P($PEGMA_{2.0}$-*co*-$MAA_{7.4}$-$EGDMA_{0.8}$)	655 100	89 300	7.34

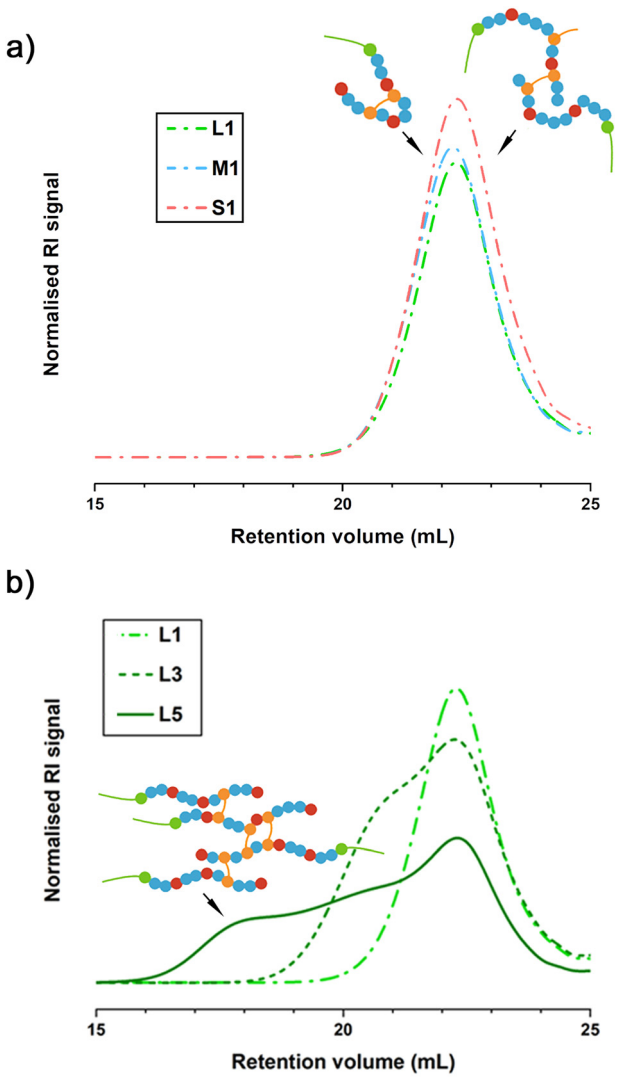

Fig. 2 (a) Overlaid TD-SEC chromatograms showing the refractive index (RI) signal against the retention volume (mL) for co-polymers synthesised at high dilution (10 wt% monomers concentration, L1, M1 and S1). Traces with broad mono modal peaks are associated with linear or cyclised co-polymers. (b) Overlaid TD-SEC chromatograms for the L-series (L1, L3 and L5) showing a considerable broadening of the traces when monomer concentration increases up to 50 wt% (for L5), which evidences an increase in branching.

perhaps be better described as linear or cyclised co-polymer surfactants (LCS).

The absence of branching in M1 and L1 co-polymerisations (involving $PEGMA_{950}$ and $PEGMA_{500}$ macromonomers) could be attributed to remaining pendant vinyl groups at monomer conversions below 95%. However, the absence of high molecular weight branched species in S1 co-polymerisation ($PEGMA_{300}$, which achieved >99% vinyl conversion and thus consumed the vast majority of pendant vinyl groups) indicates that another factor is responsible for the suppression of branching reactions. It is known that high dilution can also suppress branched co-polymer formation by selectively promoting the consumption of pendant vinyl groups through intramolecular cyclisation reactions over intermolecular branching.[36,37]

Increasing the PEGMA length provides a way to control the spatial distribution of hydrogen bond donor and acceptor motifs throughout BCSs macromolecular structures. This is because we fix an equimolar PEGMA to MAA ratio in the synthesis of BCS with different PEGMA lengths ($PEGMA_{950}$, $PEGMA_{500}$ and $PEGMA_{300}$), and the relative PEG content in each PEGMA monomer decreases with chain length (w.r.t. the monomer molas mass, 0.89, 0.80 and 0.66 respectively). Longer PEGMA monomers (L-series) provide fewer side chains sparely distributed in the co-polymer architecture, while short PEGMA monomers (S-series) can provide more and evenly distributed side chains (Fig. 3). The formation of linear BCS analogues (LCS) at high-dilution, provides an opportunity to evaluate the role of co-polymer topology in the LAOS fingerprints of BCS_{dev} formulations (in Sections 3.2 and 3.4).

3.1.2 Controlling BCS macromolecular topology. The Strathclyde methodology can promote branching reactions by increasing the stoichiometry of the bifunctional monomer to chain transfer agent ($[EGDMA]_0/[DDT]_0$) ratio or by increasing the monomers concentration during the co-polymerisation.[38] At 30 and 50 wt% monomers concentration in the reaction, the $[EGDMA]_0/[DDT]_0$ ratios have to be adjusted to prevent the formation of cross-linked 3D gel networks, that occur when excessive numbers of branching reactions exceed the percolation threshold of the Flory–Stockmayer gelation theory.[39,40]

With the simultaneous modification of both, solids content and PEGMA length, the $[EGDMA]_0/[DDT]_0$ ratio at which the mixture reaches the percolation threshold varies for each

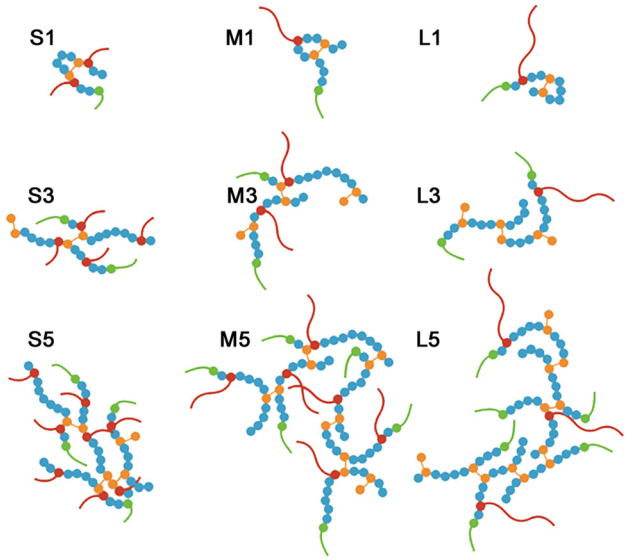

Fig. 3 Schematic representations of the proposed structures for the library of BCS derivatives synthesised in this work. High-dilution co-polymerisation (10 wt% monomers concentration) results in linear polymers (S1, M1 and L1) that are likely cyclised with a globular structure. As the monomers concentration increases, the degree of branching also increases, with an average of two primary chains for the co-polymers made at 30 wt%, 4 (S5), and 6 (M5 and L5) for those synthesised at 50 wt%. The vinyl repeat units per chain end (DDT) is very similar for all co-polymers ≈11–12.

derivative (Table 1). The shift in gelation threshold is expected in line with other methods such as transfer-dominated branching radical telomerisation (TBRT).[41] For medium and short PEGMA chains at high dilution (S1 and M1, at 10 wt% solids), the $[EGDMA]_0/[DDT]_0$ ratios that were accessible before gelation are 1.09 and 1.05 respectively (Table 1), in agreement with other reports using the Strathclyde method. As the solids content increases, co-polymerisations at $[EGDMA]_0/[DDT]_0$ = 1 for the three PEGMA macromonomers at 50 wt% solids, and for $PEGMA_{950}$ at 30 wt%, led to gel formation (due to the prevalence of excessive branching reactions). The $[EGDMA]_0/[DDT]_0$ ratio needs to drop below 1 for 30 wt% solids and under 0.85 for 50 wt% (Table 1). Adjusting this ratio enables the isolation of soluble BCS_{dev} with different PEGMA chains (S, M and L) and dilution conditions (Table 1).

Vinyl conversions for M3 and S3 co-polymerisations (conducted at 30 wt% solids and $[EGDMA]_0/[DDT]_0$ = 0.96) reach values ≥98% (Table 1), which are above the threshold for branching reactions. However, TD-SEC results show that dispersity values, Đ, vary for different PEGMA macromonomers at 30 wt% solids (4.62 and 2.26 for M3 and S3 respectively, Table 2). The RI traces for M3 and S3 also show consistent differences in branching extent and molecular weight distribution (*e.g.* M3 co-polymers are branched with a wide distribution, Table 2 and Fig. S3, ESI†). This is likely due to the inherent variation in the weight fraction of the PEG substituent, which has a considerable impact on branched co-polymer formation.[35,42]

Adjusting the $[EGDMA]_0/[DDT]_0$ ratio to 0.94 when conducting the co-polymerisation with $PEGMA_{950}$ at 30 wt% solids resulted in the formation of a soluble BCS_{dev} (L3, Tables 1 and 2). The reactions conducted at 50 wt% solids required greater reductions of the $[EGDMA]_0/[DDT]_0$ ratio to avoid the formation of cross-linked gelled networks due to extensive branching. By reducing this ratio down to 0.81–0.83 it was possible to form soluble BCS_{dev} derivatives (L5, M5 and S5 in Tables 1 and 2) at 50 wt% solids for the three PEGMA macromonomers. Increasing the monomers concentration up to 50 wt% leads to higher molecular weights (Table 2) with broader distributions (Fig. 2 and Fig. S3, ESI†). For example, despite reducing the $[EGDMA]_0/[DDT]_0$ ratio from 1.09 to 0.82, the M_n increases from 19 900 g mol^{-1} for M1 to 115 700 g mol^{-1} for M5 as the monomers concentration increases from 10 to 50 wt% (Table 2). The increase in both, molecular weight and dispersity, Đ, are characteristic of branched co-polymer formation.[43]

Considering that LCS co-polymers S1, M1 and L1, resemble the primary chains of the analogous branched species S5, M5 and L5 (formed at higher reaction concentrations), we can estimate the average number of primary chains per BCS_{dev} (by dividing M_n values by that of the equivalent LCS, *e.g.* for M3: $\frac{M_n(M3)}{M_n(M1)}$). M1, M3 and M5 contain ≈1, 2 and 6 primary chains respectively (L1, L3 and L5 show the same trends and values, Fig. 3).

Tuning the reaction conditions of the Strathclyde synthesis, enables the production of new pH responsive co-polymers containing systematic variations in spatial distribution of hydrogen bonding motifs and macromolecular topology (Fig. 3). The subtle changes in co-polymer structure can be exploited in the formation and yielding of hierarchical self-assemblies containing droplets, particles, or both.

3.2 BCS-derivatives as formulation additives to create yield stress fluids

The pH-responsive behaviour of BCSs has been exploited in drug delivery and to control the assembly of oil/water emulsions[15] and emulsified ceramic suspensions,[10,16] thus enabling the processing of advanced materials (Al_2O_3, SiC,[44] and graphene oxide[17]). BCS derivatives (S, M and L series) can aid the processing of AC and STO in water and decane:water emulsions. Each formulation shows distinctive LAOS fingerprints (Fig. S4–S7, ESI†), which serve as a first screening to select promising formulations for further study. The following rheological indicators suggest that the material exhibits a yield stress without structural disruption in the solid-to-liquid transition: (1) a minimal or absent stress overshoot in the flow transition region (or no apparent signs of structural disruption), (2) G'_{LVR} values >10 kPa (measure of material strength), (3) σ_f > 100 Pa (or "yield stress"), (4) and $FTI^{-1} \rightarrow 1$ (measure of the extent of the flow transition region) (Table 3).

3.2.1 Rheology of assembled AC suspensions. Powder properties play a critical role in the stabilisation and rheology of water-based formulations.[6,8] AC particles are difficult to process in water due to their irregular shape, wide particle distribution (Fig. S4 and S5, ESI†), large contact angle >120°, and high surface area (BET ≈ 1100 m^2 g^{-1}). After being

dispersed in a BCS-L-series stock solution, the water contact angle drops to ≈30° (Fig. S4c and d, ESI†) thanks to the electrosteric stabilisation of the surfaces provided by BCS-L molecules.

The LAOS fingerprints for all AC-BCS_{dev} formulations show that PEGMA side chain length and branching degree result in different yielding behaviours. AC formulations prepared with the linear or cyclised analogues (LCS, from co-polymerisations at 10 wt% solids, AC-S1 and AC-M1) show type I behaviour[24] and a stress overshoot in the flow transition region (between the end of the LVR and the moduli cross-over, $G' = G''$). The storage and loss moduli show a considerable standard deviation in this region (Fig. 4a and Fig. S8a, ESI†), with a noticeable stress maximum (σ_{max}) in the σ_0 *vs.* γ_0 plot (Fig. 4c and Fig. S8c, ESI†). Large uncertainty and stress overshoots are associated with microstructure disruption and flow instabilities.[22] AC-S1 and M1, both exhibit a narrow linear viscoelastic region (LVR), and high G' and G'' values, with stress overshoots of ≈250 and 500 Pa respectively. These overshoots (σ_{max}) take place at small strain amplitudes (≈3 and 5% for AC-M1 and S1 respectively, Table 3). Considering only characteristic values at the moduli-crossover could be misleading and result in the underestimation of $\sigma_{crossover}$ and the flow transition index, FTI^{-1} (that provides a measure of the extent of the flow transition region and flowability).[23,45] When a stress overshoot takes place before the moduli crossover, σ_{max} should be used as a point of reference, to define the flow transition region and the FTI^{-1} (Table 3).[22] An abrupt yielding would correspond to $FTI^{-1} \rightarrow 1$, while $FTI^{-1} \rightarrow 0$ corresponds to a gradual flow transition.[23] The FTI^{-1}, in isolation, has its own limitations to capture the underlying physical processes, but combined with other metrics helps capturing distinctive behaviours.[23] In short, with intense stress overshoots, AC-M1 and S1 formulations would be expected to cause issues during processing.

LCSs fail to produce stable gels with a consistent and smooth flow transition, while any branched BCS_{dev} (S, M and L, co-polymerised at 30 and 50 wt% solids) show similar and more reliable trends in the flow transition region (Table 3, S3, S5 (Fig. S8, ESI†), M3, M5 (Fig. 4), and L3, L5 (Fig. S9, ESI†)). Each has a well defined extensive LVR region and shows a smoother transition without intense overshoots in the σ_0 *vs.* γ_0 plots.

Branched co-polymers can form soft AC gels with low stiffness and material strength.[23] The 12-AC M3 sample stands out amongst the AC formulations (Table 3) without a stress overshoot in the flow transition region. It also shows a slight type III behaviour[24] with a G'' overshoot within the flow transition region just before the crossover (Fig. 4a). This overshoot is associated with the energy transitions (recoverable and unrecoverable processes) taking place during the yielding phenomenon.[46] This sample with $G'_{LVR} \approx 12$ kPa requires relatively small stress values to enter the non-linear regime ($\sigma_{nl} \approx 26$ Pa), which then reaches a plateau around the moduli crossover ($\sigma_{crossover} \approx 50$ Pa and $\gamma_{crossover} \approx 3\%$). The results suggest that this formulation could be used for direct coagulation casting to create complex shapes through directed assembly (Section 3.3.1). The limited amount of AC powders that can be stabilised (12 vol%) results in formulations with insufficient strength for DIW.[23]

3.2.2 Rheology of assembled STO emulsified suspensions. STO particles can be easily stabilised in a BCS-L1 (LCS co-polymer) stock

Table 3 Characteristic rheological metrics for all formulations prepared using the library of BCS_{dev} to stabilise activated charcoal (AC) suspensions and strontium titanate (STO) emulsified-suspensions. Average values (from at least two repeats) accompanied by standard deviations have been rounded up to the nearest hundred, tenth or as appropriate. σ_{nl} values for most samples have been determined from correlation data when G' falls below $90\%G'_{LVR}$ (w.r.t. a G' value within the LVR, taken at $\gamma_0 = 0.05\%$)

	Formulation	G'_{LVR} (Pa)	γ_{nl} (%)	σ_{nl} (Pa)	γ_{max} (%)	σ_{max} (Pa)	$\gamma_{crossover}$ (%)	$\sigma_{crossover}$ (Pa)	FTI^{-1} ($\sigma_{nl}/\sigma_{crossover}$)	$FTI_{max}{}^{-1}$ (σ_{nl}/σ_{max})
L-series	12-AC L3	5700 ± 100	0.15 ± 0.01	8 ± 1	2	25 ± 2	10 ± 5	20 ± 1	NA	0.3 ± 0.0
	12-AC L5	2300 ± 700	0.19 ± 0.03	3 ± 1	3 ± 1	13 ± 3	10 ± 1	10 ± 2	NA	0.3 ± 0.1
	47-STO L3	101 800 ± 30 800	0.07 ± 0.01	56 ± 8	NA	NA	22 ± 2	276 ± 44	0.2 ± 0.1	NA
[b]	47-STO L5	73 600 ± 20 900	0.13 ± 0.06	83 ± 15	NA	NA	20 ± 1	450 ± 230	0.2 ± 0.1	NA
M-series	12-AC M1	44 700 ± 13 600	0.12 ± 0.01	46 ± 11	3 ± 1	250 ± 40	12 ± 6	147 ± 16	NA	0.1 ± 0.0
[b]	12-AC M3	11 900 ± 1100	0.24 ± 0.04	26 ± 2	NA	NA	3 ± 1	50 ± 3	0.5 ± 0.0	NA
	12-AC M5	48 900 ± 7800	0.24 ± 0.01	11 ± 2	2.4 ± 0.1	22 ± 4	2.8 ± 0.3	22 ± 4	NA	0.5 ± 0.0
	47-STO M1	105 900 ± 17 200	0.07 ± 0.01	77 ± 7	NA	NA	13 ± 3	308 ± 6	0.3 ± 0.0	NA
	47-STO M3	50 200 ± 9100	0.13 ± 0.02	64 ± 1	NA	NA	16 ± 1	225 ± 24	0.3 ± 0.0	NA
	47-STO M5	23 300 ± 2800	0.39 ± 0.0	89 ± 11	NA	NA	14 ± 2	280 ± 40	0.3 ± 0.0	NA
S-series	12-AC S1	58 700 ± 1100	0.11 ± 0.01	87 ± 40	5 ± 1	510 ± 320	20 ± 8	212 ± 88	NA	0.2 ± 0.0
	12-AC S3	7800 ± 800	0.11 ± 0.01	7 ± 1	1.2 ± 0.1	17 ± 1	2.0 ± 0.2	16 ± 1	NA	0.4 ± 0.0
[a]	12-AC S5	7500 ± 1500	0.07 ± 0.0	16 ± 5	2 ± 0	23 ± 0	2.7 ± 0.2	31 ± 8	NA	0.5 ± 0.0
	47-STO S1	40 300 ± 2700	0.07 ± 0.0	28 ± 2	NA	NA	9 ± 2	133 ± 4	0.2 ± 0.0	NA
	47-STO S3	24 600 ± 1300	0.09 ± 0.01	23 ± 1	6 ± 1	115 ± 1	12 ± 1	108 ± 2	NA	0.2 ± 0.0
[a]	47-STO S5	31 600 ± 4800	0.08 ± 0.01	25 ± 6	14 ± 1	117 ± 14	14 ± 4	132 ± 18	NA	0.2 ± 0.0
DIW	47-STO L5(2) pH ≈ 11	483 500 ± 53 000	0.10 ± 0.02	460 ± 130	3 ± 1	1820 ± 570	4 ± 1	1670 ± 450	NA	0.3 ± 0.0
DIW	47-STO L5(2) pH ≈ 3	481 100 ± 207 700	0.12 ± 0.03	570 ± 360	1.5 ± 0.4	1300 ± 820	8 ± 2	650 ± 270	NA	0.4 ± 0.0

[a] Stress overshoot in the σ_0 *vs.* γ_0 plot only takes place in one of the runs. [b] Selected formulations for Section 3.3.

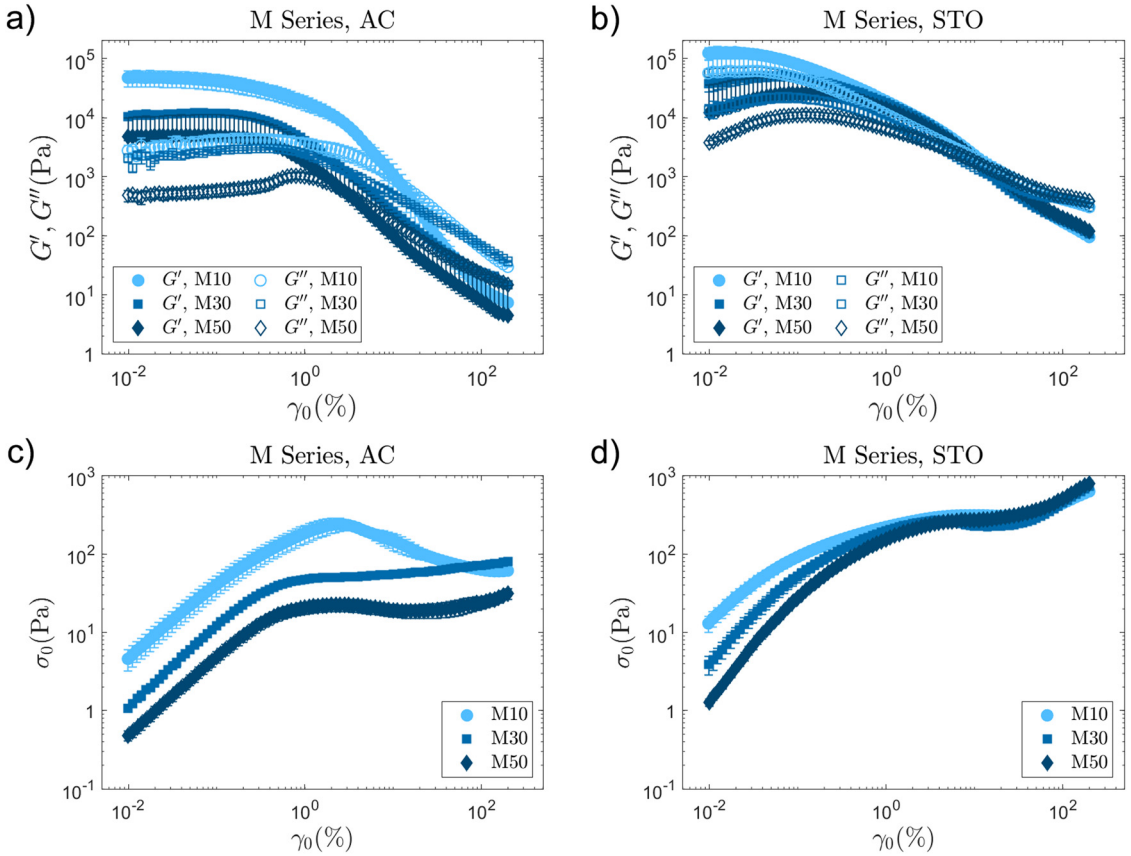

Fig. 4 LAOS results for the M-Series BCS_{dev} formulations for both materials, AC and STO. Graphs in (a) and (b) include the evolution of storage (G') and loss moduli (G'') in the amplitude sweep for AC and STO respectively. Plots in (c) and (d) show the evolution of σ_0 with increasing maximum strain amplitude γ_0 for AC and STO respectively. Linear co-polymer analogue (M1) combined with AC shows a characteristic overshoot in the flow transition region. STO-M series formulations show similar LAOS fingerprints with very subtle differences.

solution. The electro-steric stabilisation of STO particles facilitates dispersion of large aggregates that form in the absence of BCS molecules (Fig. S6, ESI†). STO powders are hydrophilic with small water contact angle ($\approx 15^{\circ}$), have a narrow size distribution around a median diameter of ≈ 2 μm, and BET values of 6.5 gm^{-2}. These properties make STO an ideal material for processing in water with BCSs, similarly to Al_2O_3,[10] and unlike AC particles (Section 3.2.1).

STO emulsified suspensions exhibit behaviours and trends that differ from those observed for AC formulations (S, M and L series in Fig. 4, Fig. S8 and S9 respectively, ESI†). This evidences that the variations in BCS_{dev} co-polymer architecture play different roles depending on the interfaces (particles and/or droplets) that the BCS_{dev} molecules are stabilising. The rheological properties of AC and STO formulations will vary with the nature of the interfaces involved, and the interactions that emerge between BCS molecules and those interfaces. In AC formulations, BCS_{dev} macromolecules only interact with AC particles (large, irregular shapes, hydrophobic, with high surface area). However, in STO formulations (emulsified suspensions) there are two types of BCS_{dev}–surface interactions, on STO particles and decane droplets. The latter provides anchoring points for the DDT chain ends in BCS molecules, thus helping with the stabilisation of the emulsion (Section 3.3).

LAOS results for STO formulations are consistent and reproducible with small standard deviations (Fig. 4b, Fig. S8b and S9b, ESI†). Most STO samples in this library do not show a stress overshoot in the flow transition region (Table 3). For each PEGMA length series (S, M and L), the branching degree does not seem to have a strong impact on formulation properties (Fig. S8b and S9b, ESI†). The σ_0 *vs.* γ_0 plots also follow similar trends within each series (Fig. 4d, Fig. S8d and S9d, ESI†). However, increasing the PEGMA side chain in branched co-polymers leads to an increase of material strength, perhaps due to the ability of the branches to reach further to establish a network. The STO-L5 formulation with $G'_{LVR} \approx 74$ MPa and $\sigma_{crossover} \approx 450$ Pa meets the material strength criteria,[23] thus showing potential for DIW. This formulation is further optimised and studied in Sections 3.3.2 and 3.4.

3.3 Shaping BCS-derivative formulations

BCSs enable the controlled aggregation of decane:water emulsions (Fig. 5a).[14–16] Using Nile red (NR) as a probe and fluorescence microscopy, it is possible to track the droplets and visualise changes in the microstructure due to the pH-triggered assembly (Fig. 5c and d). At pH values above the pK_a, small fluorescent droplets are well dispersed in the diluted

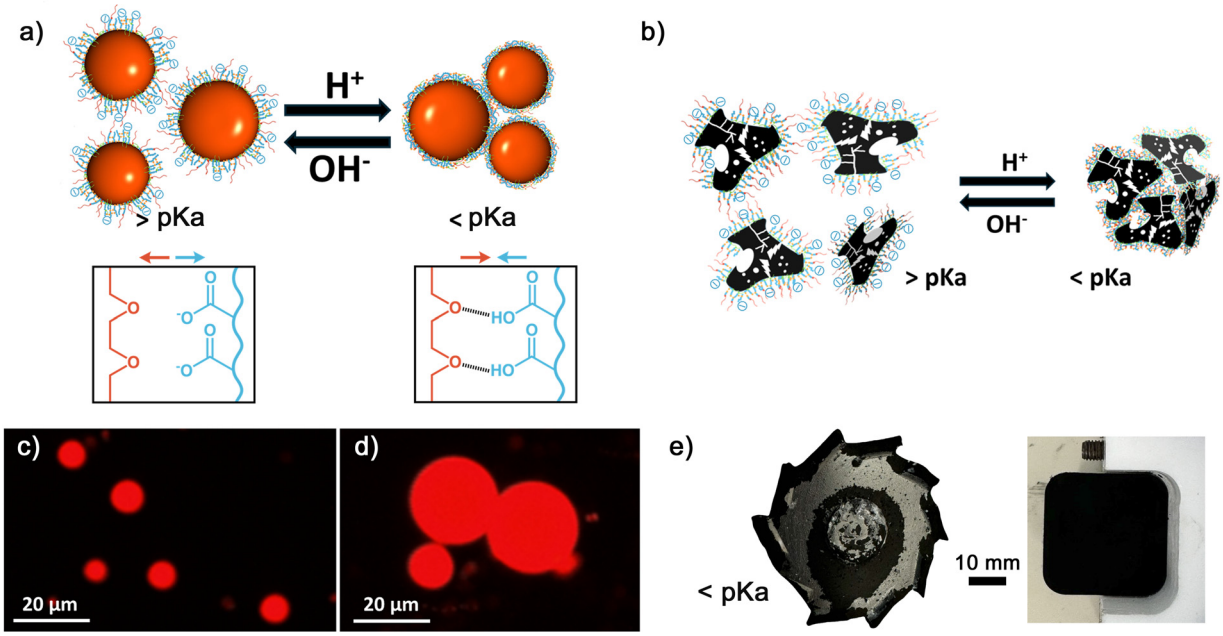

Fig. 5 (a) Scheme illustrating the pH-responsive assembly behaviour of a decane:water emulsion, with insets showing de-protonated MAA groups at pH values above pK_a, and hydrogen bond formation above the pK_a. (b) Scheme of the interactions taking place between BCS-M3 and activated charcoal surfaces. (c) and (d) Fluorescence microscopy images of BCS-L5 stabilised decane droplets probed with Nile red (NR) in basic (c) and acidic (d) conditions, evidencing that the droplets assemble into clusters in an acidic environment. (e) Images of 3D parts fabricated through direct coagulation casting of an activated charcoal suspension (12-AC M3) after triggering particle assembly using GδL to lower the pH.

continuous phase (Fig. 5c), when dropping the pH below the pK_a, the droplets assemble into clusters (Fig. 5d). This controlled aggregation is exploited to shape AC and STO in macroscopic structures through direct coagulation casting (Section 3.3.1) and DIW (Section 3.3.2).

3.3.1 Casting activated charcoal. BCSs pH responsive behaviour facilitates the controlled aggregation of AC particles, resembling direct coagulation casting techniques to create complex ceramic shapes.[1,10,16,47] The 12-AC M3 formulation (Table 3) is selected owing to its smooth flow transition (Section 3.2.1) and G'_{LVR} values. At pH values above the pK_a, the PEGMA and MAA side chains provide a electro-steric barrier, while the DDT chain ends interact with hydrophobic AC surfaces (Fig. 5b), reducing the contact angle (Fig. S5, ESI†). The addition of GδL immediately prior pouring the formulation into a mould, enables to form a gel to create macroscopic structures (12-AC M3 sample). The dry gel easily detaches from the walls (Fig. 5e).

3.3.2 Direct ink writing of strontium titanate. Branched copolymers with high molecular weight (BCS L5, Table 2) can stabilise STO emulsified suspensions (Section 3.2.2) with promising rheological characteristics (Table 3) for DIW (Fig. 6 and 7). BCSs molecules can partition in both surfaces, anchoring on decane droplets and interacting with STO particles (Fig. 6a). It is also possible that the STO particles play a role in stabilising the decane:water interface as Pickering emulsifiers.[16] The fluorescent probe (NR) can be used to qualitatively track the microstructure using fluorescence microscopy. The images of a diluted 47-STO L5 emulsified suspension evidences the stabilisation of both particles and droplets in the diluted continuous phase (Fig. 6) above the pK_a. Small decane droplets with an average diameter of ≈3 µm are well dispersed. Fluorescent STO particles with even smaller sizes can also be identified (Fig. 6b). Triggering the assembly in an acidic environment leads to the

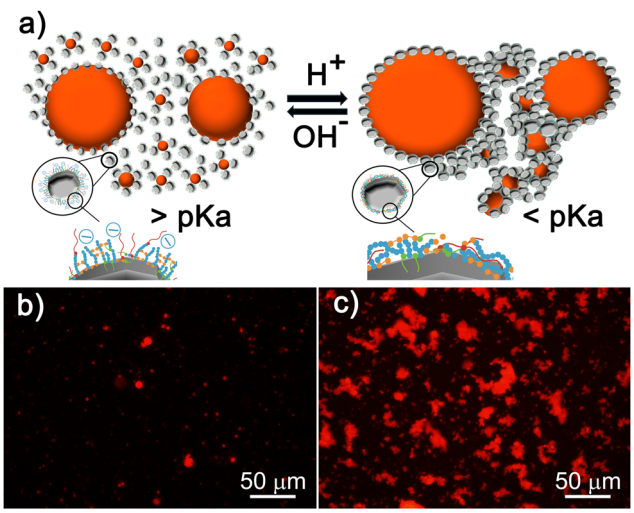

Fig. 6 (a) Schematic illustration of the pH-responsive behaviour of an STO emulsified suspension showing the interactions taking place between BCSs and the surfaces of STO particles and decane droplets. (b) and (c) Fluorescence microscopy images of diluted (1 : 100) STO emulsified suspensions at pH = 10.9 (b) and pH = 3 (c). The images evidence the responsive behaviour: above the pK_a, NR-tagged oil droplets and STO particles are dispersed in the diluted continuous phase (b). At pH < pK_a, the activation of hydrogen bonds leads to aggregation and cluster formation (c).

formation of particle aggregates and clusters of particles and droplets (Fig. 6c).

Increasing the BCS-L5 concentration up to 2 wt% (while maintaining the other formulation parameters) leads to the formation of a gel-like soft material during the emulsification process, which can form free standing shapes. The 47-STO L5(2) formulation emulsified with a 60 : 40 (suspension : decane) ratio forms a physical gel owing to the interplay between surfactant and particle stabilisation.[16,48,49] Although the pH-switching behaviour is not activated, BCSs molecules play a critical role facilitating the processability of STO particles through electro-steric repulsions. The combination of both (increased BCSs and high particle concentration) provide favourable conditions to achieve a very stable emulsion gel with material strength that enables 3D shaping. This gel can be directly used in DIW to produce parts with good printing resolution (Fig. 7a–c). *In situ* monitoring demonstrates that this formulation flows without signs of microstructure disruption at the tip and that it can be deposited to create self-supporting complex shapes (Fig. 7a and b). SEM images show that the filaments retain their shape and dimensions with good print quality (Fig. 7c).

Reducing the pH of this formulation to ≈3, either using GδL (Fig. S10, ESI†) or HCl, leads to an heterogeneous material with granular texture. *In situ* monitoring during the DIW process shows that this formulation does not flow steadily, showing signs of phase separation (large oil droplets), clogging, and over-extrusion that take place randomly. The unsteady flow results in poor shape fidelity (Fig. 7d and e). SEM images confirm the loss of printing resolution, with distorted filaments and pores between them (Fig. 7f). The results suggest that the pH-triggered assembly, and activation of inter-molecular hydrogen bonds, lead to the disruption of the physical gel achieved through electro-steric stabilisation at high pH. The controlled aggregation results in microstructural changes that compromise the flow behaviour. Image analysis of pore sizes in SEM images evidence that the decane droplets coalesce due to the de-stabilisation of the physical gel. By measuring the pore sizes from SEM images taken on dry samples after printing, it is possible to estimate that the average droplet size at pH ≈ 11 is ≈3 ± 1 μm, which increases up to ≈8 ± 4 μm at pH ≈ 3 due to de-stabilisation and coalescence.

Although the pH-responsive behaviour cannot be exploited exactly as expected, branched co-polymer surfactants with long PEGMA side chains can aid the formation of a physical gel for DIW. A detailed rheological analysis to compare the yielding behaviour of the 47-STO L5(2) formulation before and after controlled assembly is presented and discussed in Section 3.4.

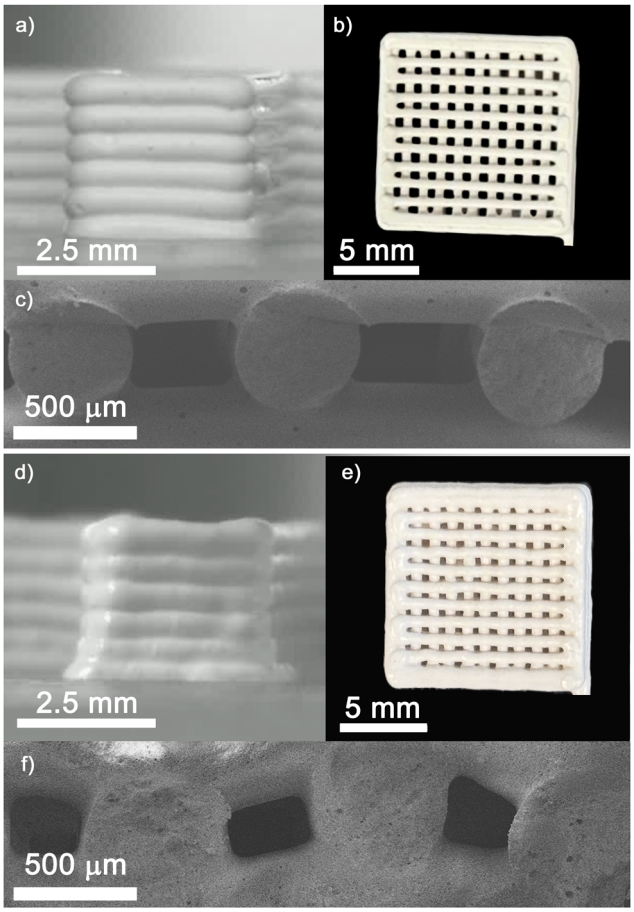

Fig. 7 *In situ*-monitoring images during the DIW process and SEM images showing qualitative differences on print quality for STO formulations before (pH ≈ 11 (a)–(c)) and after (pH ≈ 3 (d)–(f)) assembly. Both formulations can be used to create 3D lattices and other shapes, however they lead to different printing resolution. The STO formulation at pH ≈ 11 (a)–(c) is printable and produces shapes that retain the pre-designed features, such as macropores in the lattice (b) and filament shape (c). However, triggering the assembly driven by hydrogen bond formation between BCS molecules (at pH ≈ 3, (d)–(f)) compromises print quality.

3.4 Linking LAOS fingerprints and printing behaviour

DIW feedstocks are yield stress fluids which undergo transient yielding and re-structuring during the printing process (Fig. 8a). The material's response during the DIW process can be generally described using dimensionless groups to facilitate comparisons.[50] The Deborah number (De) distinguishes the extent of a material's rheological response between viscous and elastic at a given time frame, thus De → ∞ for purely elastic solids, and → 0 for purely viscous fluids.[51] The Weissenberg number (Wi) is often defined as the product of the relaxation time and the characteristic rate of deformation and can be interpreted as a measure of the strength of the flow.[50] The DIW process can be described as a transition between solid-like (De↑ and Wi↓) and flowing liquid (De↓ and Wi↑) responses when the material is subjected to different strains and deformation rates (Fig. 8a). Assuming that the response of the flowing material follows a simple power-law model,

$$\tau = K\left(\frac{\mathrm{d}u}{\mathrm{d}y}\right)^n \quad (1)$$

where, τ is the stress, K is the consistency coefficient, u is the velocity, and n is the flow index (n = 1 Newtonian, <1 shear thinning, and >1 shear thickening fluids). And considering ideal flow conditions through the tip of the nozzle (steady state,

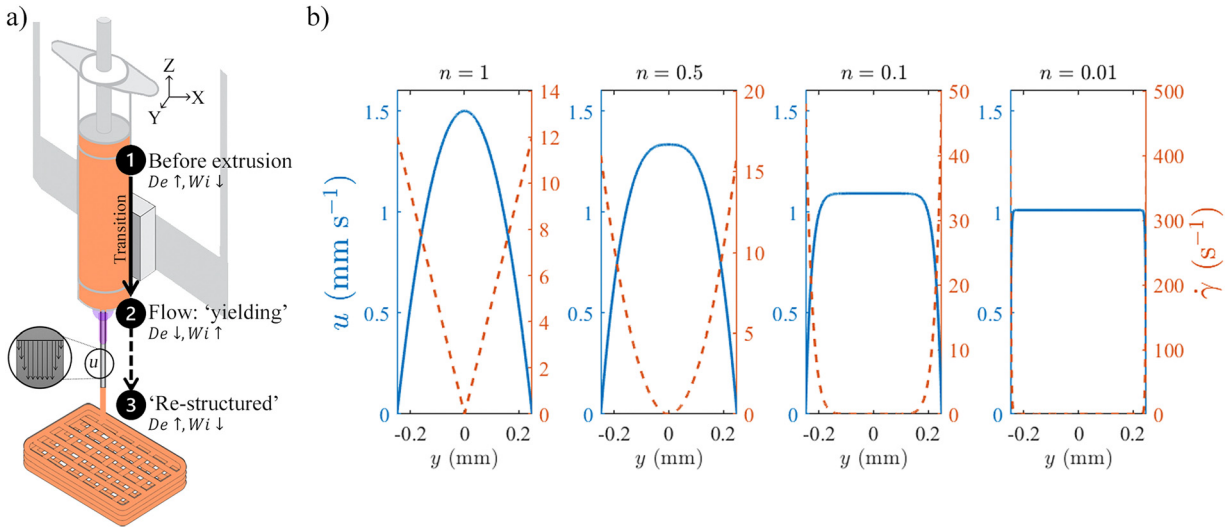

Fig. 8 (a) Schematic of the DIW process showing the different states of the material: (1) solid state before extrusion, or above the yield stress, (2) liquid-like state during flow, or below the yield stress, and (3) solid-like state once deposited, which should be above the yield stress. The material undergoes transient and non-linear behaviours between 1 → 2, and 2 → 3. The material's properties and responses can be described using the Deborah (De) and Weissenberg (Wi) numbers.[50] (b) Velocity (u, mm s^{-1}) and shear rate ($\dot{\gamma}$, s^{-1}) profiles calculated for different n values assuming idealised flow conditions and a simple power law behaviour (eqn (1) and (2)).

$\frac{\partial u}{\partial t} = 0$, fully developed, $\frac{\partial u}{\partial x} = 0$, and laminar flow with very small Reynolds numbers, $\mathrm{Re} = \frac{\rho u D}{\eta} \ll 1$), a simple dimensionless velocity profile can be obtained by applying a force balance or deriving a reduced form of the Hagen–Pousiuelle equation,[52]

$$\frac{u}{u_0} = 1 - \left[\frac{y}{r}\right]^{\frac{(n+1)}{n}} \quad (2)$$

where u/u_0 is the dimensionless velocity, u_0 is the maximum velocity at $y = 0$, n is the flow index, and y/r is the dimensionless height from the center of the nozzle tip. This dimensionless velocity profile shows that the shape of the velocity profile depends on n. For a Newtonian fluid ($n = 1$) the profile becomes parabolic, and for shear-thinning fluids ($n < 1$) the velocity profile becomes flatter in the center, with a steeper gradient near the wall. As $n \to 0$ $\dot{\gamma}$ increases considerably (Fig. 8b). In practice, extrusion flows are complex and likely heterogeneous, while the behaviour of the material should be represented using models able to capture the complex features above and below the yield stress.[53,54] However, elucidating realistic processing conditions or modeling the behaviour of STO emulsion gels is beyond the scope of this manuscript. Although it is often argued that flow conditions under oscillatory tests are not representative of the DIW process, LAOS can capture distinctive behaviours, and provide results with smaller uncertainties[45] to determine characteristic metrics that correlate with printing resolution.[22,23]

Steady shear experiments have been used to study the flow behaviour of similar DIW feedstocks.[55] Other studies on ceramic emulsions for DIW focused on oscillatory tests.[56] Although not commonly reported and discussed in the field, the experimental data collected in continuous shear can be unreliable for printable materials.[45] Attempts to perform a continuous shear test on our STO gels (even at shear rates between 0.0001 and 1 s^{-1}), have led to measurement issues and flow instabilities (Fig. S11, ESI†). The emulsions are expelled from the gap before a steady state can be reached, while microscopy images show shear banding and fracture (Fig. S11, ESI†). From steady shear results for the STO physical gel, it could be assumed that $\tau_y^{dyn} \approx 350 \pm 50$ Pa, and the flow index $n \to 0$. However, steady shear does not differentiate the subtleties between the two samples, with the added limitation that these results are knowingly affected by flow instabilities.

The analysis of both transient and correlation data from LAOS experiments (Section 2.7), using complementary mathematical frameworks,[23,25,27,30] enables the quantification of characteristic properties (G'_{LVR}, γ_{nl}, σ_{nl} and $\sigma_{crossover}$), and their evolution in the flow transition region (G', G'', σ_0, $\frac{I_3}{I_1}$, ϕ). These quantitative metrics and their trends, combined with visual analysis of Lissajous–Bowditch (Fig. 11) and Cole–Cole plots (Fig. 12), are able to capture distinctive features of the underlying yielding process for each STO formulation (before and after aggregation).

3.4.1 G', G'' and σ_0 evolution with strain amplitude γ_0. Although both formulations show similar trends on G', G'' and σ_0 values with increasing strain amplitude, γ_0, there are quantitative differences between them (Fig. 9). Both samples show a type I behaviour:[24] storage and loss moduli gradually decrease with increasing strain amplitude. Their stress curves also follow similar trends, deviating from a linear relationship before reaching a maximum value in the flow transition region (σ_{max}, Fig. 9 and Table 3). The LAOS results for the STO physical gel

(pH ≈ 11) are fairly consistent with some deviation between transient and correlation values around the moduli crossover. However, the aggregated STO formulation (pH ≈ 3) shows considerable deviations at any γ_0 value (Fig. 9). The data discrepancy between repeated measurements for the aggregated STO formulation can explain the unsteady flow behaviour observed during printing (Section 3.3.2). σ_0 values for the physical gel reach a maximum (σ_{max}) close to the moduli crossover (Fig. 9a) with $\gamma_{max} \approx 3\%$ and $\gamma_{crossover} \approx 4\%$ and corresponding stress values $\sigma_{max} \approx 1820 \pm 570$ Pa and $\sigma_{crossover} \approx 1670 \pm 450$ Pa (Table 3). However, the aggregated formulation (at pH ≈ 3) shows an overshoot ($\sigma_{max} = 1300 \pm 820$ Pa) at smaller strains ($\gamma_{max} = 1.5 \pm 0.4\%$), and an intense stress drop at the crossover ($\gamma_{crossover} = 8 \pm 2\%$ and $\sigma_{crossover} = 650 \pm 270$ Pa, in Table 3, and Fig. 9b). The large uncertainty of LAOS results for this sample (Table 3) and the intense stress drop after the maximum value (Fig. 9b) highlight potential microstructure disruption events (*e.g.* breaking of the emulsion, phase separation, jamming, slip *etc.*) that are inconsistent between runs.[22] Additional rheological metrics and analyses can provide further insights into the underlying physical processes and/or flow instabilities taking place (Sections 3.4.2 and 3.4.4).

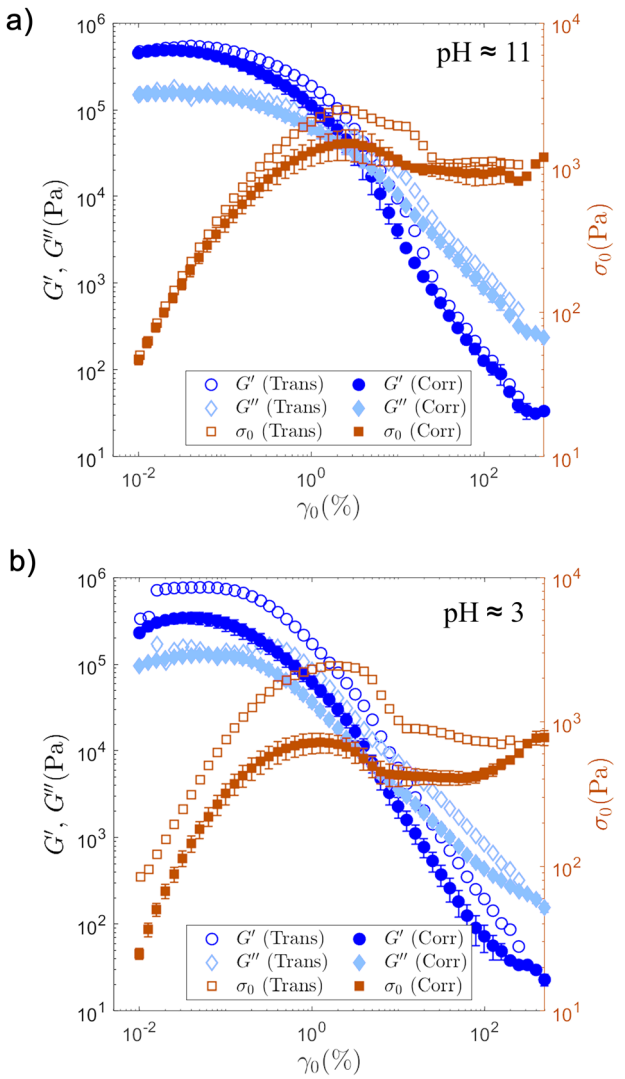

Fig. 9 LAOS results. G', G'' and σ_0 evolution with increasing strain amplitude γ_0 for the 47-STO L5(2) emulsified suspensions before (a) and after (b) pH-triggered aggregation (with pH values of ≈11 and 3 respectively). The graphs include results from correlation (calculated by the TRIOS software, filled symbols) and transient measurements (from our analysis of raw data signals, empty symbols).

3.4.2 Onset (γ_{nl}, σ_{nl}) and evolution of non-linearities $\left(\frac{I_3}{I_1}\right)$. The analysis of nonlinearities captures characteristic fingerprints that correlate with printing behaviour. The higher harmonics maps obtained through FT analysis show clear differences in the non-linear behaviours before and after aggregation (Fig. 10). For the physical get at pH ≈ 11, the onset of non-linearities ($n = 3$, $\frac{I_3}{I_1} > 0.01$) takes place at $\gamma_{nl} \approx 0.13\%$ (from the FT analysis, Fig. 10). Only odd harmonics gradually rise with increasing strain amplitude (Fig. 10a). At large amplitudes approaching 100%, there are some subtle signals of the second harmonic. However, the aggregated STO formulation, at pH ≈ 3, shows intense odd and even harmonics (Fig. 10b) with an onset of $\frac{I_3}{I_1} > 0.01$ at $\gamma_{nl} \approx 0.16\%$ (from the FT analysis). Intense even harmonics have been associated with wall slip,[57] and with stress heterogeneities in a material system.[49,58] The non-linear parameter $\frac{I_2}{I_1}$ has been found to increase when defects appear in a polymeric material subjected to a fatigue test in non-linear conditions;[58] the even harmonics become not negligible when cracks form and propagate. It has also been associated to phase-separation of oil:water emulsions stabilised by clay particles.[49] Considering that the $\frac{I_2}{I_1}$ non-linear parameter can be used as an indicator of phase separation in relation to emulsion stability,[49] the higher harmonics fingerprints (Fig. 10) provide strong evidence to support our microstructure disruption hypothesis. The STO formulation at pH ≈ 3 shows intense $I_{2/1}$ and $I_{3/1}$ and higher harmonics (Fig. 10b), they reach a maximum and suddenly drop to a minimum at $\gamma_0 \approx 10\%$. From this point, the second harmonic remains low while the third raises again. This shift in trends for both is similar to those observed in fatigue tests performed on polymeric materials,[58] and for oil:water emulsions stabilised with hydrophobic clays.[49] Other emulsion gel systems do also show a maximum value of $I_{3/1}$ at increasing strain amplitude.[59,60]

The harmonic maps and trends on non-linear parameters $I_{2/1}$ and $I_{3/1}$ are consistent with stable and unstable systems in literature.[49,59] The FT analysis provide fingerprints and quantitative evidence of distinctive behaviours before and after the pH-triggered assembly.

3.4.3 Elastic Lissajous–Bowditch plots. The elastic LB plots complement the findings from the FT fingerprints showing that both samples are very similar within the LVR and at very large amplitudes ($\gamma_0 \approx 250\%$). However, their elastic LB curves are clearly distinctive in the flow transition region where the aggregated STO emulsified suspension (47-STO L5(2) pH ≈ 3, Table 3) displays asymmetric curves at intermediate values of γ_0

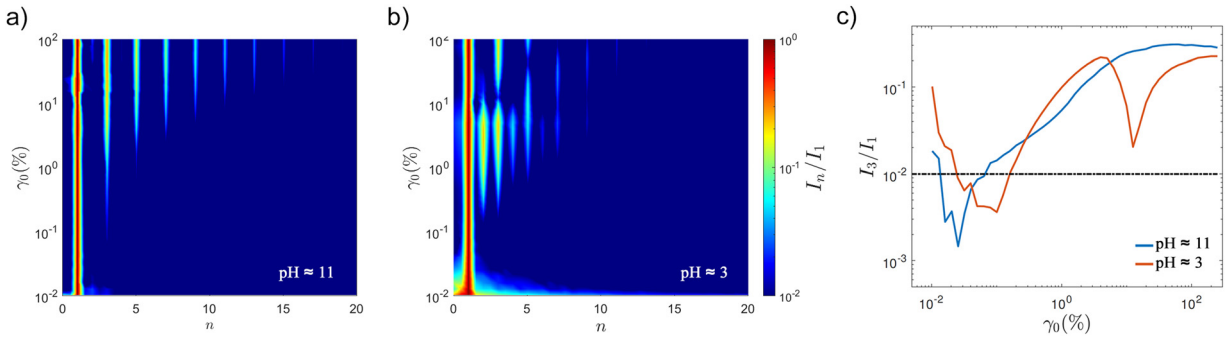

Fig. 10 (a) and (b) FT maps of higher harmonics (n) for STO formulations before and after triggering the assembly using HCl, at pH values ≈11 and 3 respectively. The aggregated STO formulation has intense even harmonics and non-linearities at small strain amplitudes. (c) The evolution of the relative intensity of the third w.r.t. the first harmonic $\left(\frac{I_3}{I_1}\right)$ shows distinctive trends for the two samples.

between ≈0.15 and 10%. This strain space coincides with the raising of the second harmonic ($I_{2/1}$, Fig. 10b). The asymmetry of LB curves is also associated with emulsion instability.[49] The LB plots for the printable physical gel (formed during emulsification at high pH) show a similar evolution to the observed for pluronic F127 hydrogel,[22,23] commonly used in DIW. The STO emulsion gel displays a typical visco-elastic elliptical LB curve in the LVR (Fig. 11), which becomes distorted with the rising on non-linear behaviours. As γ_0 increases to values beyond the moduli crossover, the LB plot gets closer to a square shape associated with (in principle, from a bulk perspective) an "ideal" yield stress behaviour.[30] However, this sample also shows asymmetries in the LB curves under large deformations (Fig. 11, γ_0 = 49.9 and 249.9%), where the corners deviate from the ideal square shape and reveal the subtle asymmetry. This is in good agreement with the FT fingerprints that show signs of the second harmonic at large strain amplitudes (Fig. 10a). The visual information provided by the Lissajous–Bowditch plots complements the FT analysis, however, further analysis of local flows and micro-structural changes are needed to explain the bulk results at large amplitudes.

3.4.4 ϕ evolution and SPP inter-cycle trajectories. The dissipation ratio trends and the SPP fingerprints also highlight the differences in the yielding process (Fig. 12). ϕ values for the physical gel at pH ≈ 11 show a gradual evolution increasing from ≈0.25 to ≈0.89 in the flow transition region.[30,61] This evolution is similar to ϕ trends observed in hydrogels[22] and Pickering emulsions.[61] However, for the aggregated

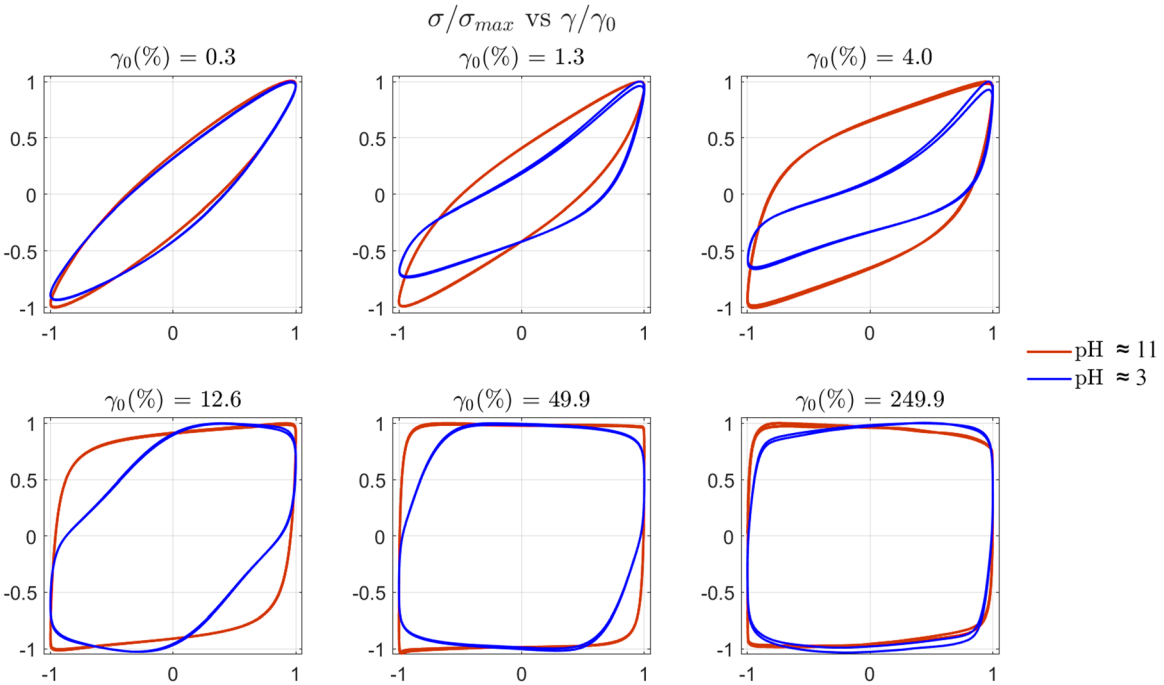

Fig. 11 Normalised elastic Lissajous–Bowditch (LB) plots (σ/σ_0 *vs.* γ/γ_0) for STO formulations: STO47 L5(2) at pH ≈ 11 and ≈3 before and after aggregation respectively. LB curves for the aggregated sample at pH ≈ 3 are asymmetric at intermediate values of strain amplitude that correspond to the increase of even harmonics, $I_{2/1}$ in Fig. 10(b), between γ_0 ≈ 0.015 and 10%.

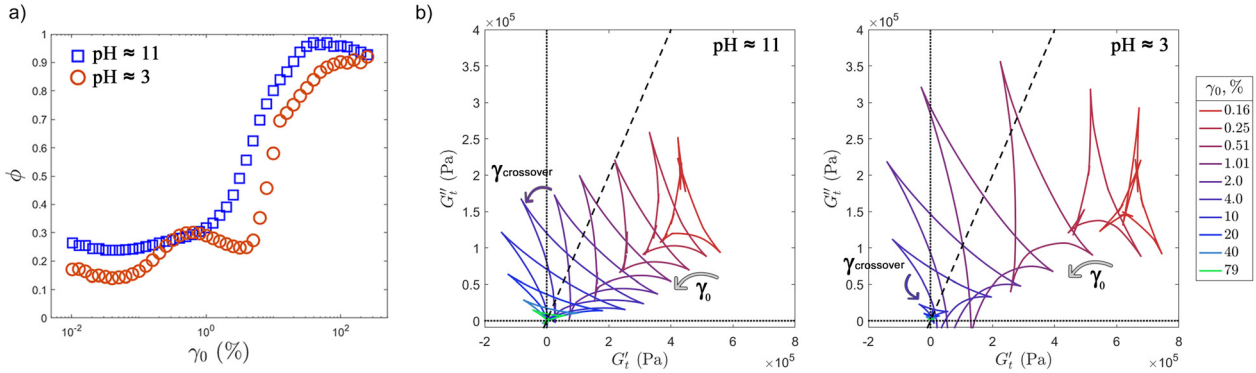

Fig. 12 (a) Dissipation ratio (ϕ) evolution with γ_0 for both STO samples before and after aggregation, at pH ≈ 11 and 3 respectively. (b) SPP Cole–Cole plots showing the inter-cycle trajectories for STO formulations before and after triggering the assembly of BCS-L5 using HCl. The acidification changes the yielding behaviour and the extent of microstructural arrangements.

formulation at pH ≈ 3, ϕ values follow a non-monotonic trend in this region, showing a maximum value at small strain amplitudes ≈1.5% coinciding with γ_{max} (Fig. 12a). It then increases showing at least two differentiated slopes around $\gamma_{crossover}$ (Table 3). Although at very large amplitudes (γ_0 = 250%), both formulations display similar ϕ values (≈0.9), the energy dissipation in the flow transition region is clearly distinctive (Fig. 12a). However, it must be noted that it is not possible to determine and compare the nature of these energy transitions: when $0 < \phi < 1$ could mean that a particular response is somewhat plastic, or not plastic at all. The inconsistent evolution of ϕ values draws the same conclusions derived from the FT analysis. The pH-triggered assembly compromises the microstructure of the physical gel and changes its dynamic behaviour and the energy transitions that occur in the yielding process.

The inter-cycle trajectories in the Cole–Cole plots (Fig. 12b) for both samples exhibit the characteristic deltoid shapes, reflecting the dominance of the third harmonic.[29,46] However, the progressive changes in shape, orientation and enclosed area of these deltoids with increasing strain amplitude take place differently for each sample. These features offer additional insights into the sequence of microstructural rearrangements each material undergoes. A large area is indicative of a broad extent of micro-rearrangements, while the position and tilt can provide information about the energy transitions (*e.g.* predominantly elastic or viscous) and intra-cycle processes associated with changes in G_t'' and G_t' (*e.g.* thickening ↑, thinning ↓, stiffening → and softening ←).[27,29]

The inter-cycle trajectories for the gel at pH ≈ 11 show a very gradual transition in location, size of enclosed areas and tilt. The deltoids gradually move left and downwards in the Cole–Cole plot (↙ in Fig. 12b), remaining in the predominantly elastic region up to amplitude strains of ≈2%. The area of these deltoids increases very slightly with the onset of non-linearities, and it then remains fairly constant until the trajectories move into the "backflow" region[27] on the left of the Cole–Cole plot (Fig. 12b, pH ≈ 11). At strains above $\gamma_{crossover}$ ≈ 4%, the enclosed areas decrease with increasing strain amplitude, entering the predominantly viscous region within each cycle, and until the deltoids collapse with G_t' and G_t'' values → 0 Pa, reflecting the break down of the microstructure at very large amplitudes.[61]

The aggregated sample at pH ≈ 3 undergoes different physical processes throughout the amplitude sweep and within each cycle. The enclosed area in the deltoids at any given strain amplitude is larger, thus evidencing a greater extent of microstructural rearrangements. The shape of the deltoids is also different, with very sharp and narrow trajectories that enter the predominantly viscous and recoil regions at smaller strains γ_0 → 1%, thus reflecting that the physical processes that the sample undergoes in each cycle are also different. The enclosed areas reach a maximum at γ_0 ≈ 1%, and from this point, the trajectories enter the "backflow" region with negative G_t'' values. At the moduli crossover, γ_0 ≈ 8%, the deltoid has considerably shrunk and approaches the visco-plastic deformation limit.[62] Additional comparison of intra-cycle trajectories for both formulations is included in the ESI† (Fig. S12).

Overall the inter-cycle trajectory evolution provides further evidence of the distinctive physical processes that the formulations undergo before and after aggregation, which correlate with printing behaviour. The SPP trajectories and the FT fingerprints (including even harmonics) provide complementary quantification of the microstructure disruption caused by the activation of the pH-triggered assembly. The LAOS analyses can capture the changes in the gel microstructure associated with printing performance showing that yielding plays an important role in DIW. Additional aspects must be considered to assess the printability of DIW feedstocks, including: the quantification of thixotropy or re-structuring timescales,[23] extensional properties,[63] and the impact of process parameters.[32] These aspects are the subject of ongoing studies in our group and will be reported in the future.

4 Conclusions

Bringing together polymer chemistry, formulation and rheology, we have demonstrated that pH responsive branched copolymer surfactants (BCSs) can aid the design of yield stress fluids for advanced materials manufacturing.

The synthesis of pH responsive branched co-polymer surfactants has been optimised to enhance the control over co-monomer distribution and topology. By increasing the solids in the co-polymerisation reaction from 10 to 50 wt%, it is possible to enhance branching. While the use of PEGMA macro-monomers with different chain lengths provides control over molecular weight and the spatial distribution of hydrogen bonding motifs in BCSs macromolecules. Through modifications in the conditions of co-polymerisation reactions *via* the Strathclyde methodology, this work provided a library of BCS derivatives, from linear analogues to branched architectures that can be exploited to create a wide range of yield stress fluids with different rheological characteristics and yielding behaviours.

Some of these soft materials have been successfully shaped through casting and DIW to create macroscopic structures made of activated charcoal and strontium titanate. We have found that when using a branched and high molecular weight BCS (L5) under certain conditions, it is possible to achieve a stable emulsion gel through electro-steric and particle stabilisation in the absence of inter- and intra-macromolecular hydrogen bonds. The resultant soft material can be used in DIW to create complex shapes with good printing resolution. However, when trying to enhance the strength of this stable emulsion gel through pH-triggered assembly below the pK_a, this instead led to the damage of the microstructure and as a consequence to poor printing resolution.

Advanced LAOS analyses could capture distinctive fingerprints for the stable and disrupted emulsion gels, thus finding a correlation between their yielding processes and printing behaviour. FT fingerprints and the trends of the second and third harmonics evidenced that the disrupted gel undergoes phase separation during its flow transition. The dissipation ratio trends and the SPP framework provided complementary quantification of the underlying yielding phenomena.

The optimised gel can be successfully used in DIW to create complex structures with controlled features. The formulation determines the final microstructure and micron size pores of the printed filaments, while the 3D computer aided design can control the macro-porosity. These STO complex structures with potential for electrochemical applications, exemplify what can be achieved by bringing together polymer chemistry, formulation design and rheology of complex fluids. Overall, this work shows how to exploit branched co-polymer surfactants in emulsion engineering and advanced materials processing.

Author contributions

Conceptualization (EGT). Experimental work (EJ, ZL, SF, MC). Data curation (EJ, ZL, RA, SF, WS, EGT). Formal analysis (RA, SF, WS, EGT). Funding acquisition (EGT). Investigation (All). Methodology (EJ, SF, RA, EGT). Project administration (EGT). Resources (EGT). Software (EGT, RA, Freeware package by Prof Simon Rogers). Supervision (EGT). Writing original draft manuscript (EGT). Editing (EGT, WS).

Data availability

Some of the data and analyses supporting this article have been included as part of the ESI.† The raw and curated data for the co-polymers characterisation, rheological measurements and their analyses can be made available upon acceptance and request. The FT analysis has been made using our own MATLAB script, that can also be made available upon acceptance and request. The SPP analysis has been made using MATLAB functions provided by Simon Rogers (SPP Freeware package) as stated in the manuscript.

Conflicts of interest

There are no conflicts to declare.

Acknowledgements

This work was supported by a UKRI Future Leaders Fellowship MR/V021117/1. EJ was supported by a PhD studentship from The Leverhulme Research Centre for Functional Materials Design. We thank Prof. Simon Rogers for providing us with the SPP Freeware package to carry out the SPP analysis. We would like to acknowledge the use of characterisation facilities (GPC, ^{1}H NMR, SEM, Mastersizer, Contact Angle and ARES G2 TA Rheometer) within the Open Access Area of the Materials Innovation Factory at the University of Liverpool; created as part of the UK Research Partnership Innovation Fund (Research England) and co-funded by the Sir Henry Royce Institute. EGT and ZL acknowledge Mr Jack Li for their assistance in lab work during the review process. EGT acknowledges Dr Patrick Spicer and Prof. Simon Rogers for useful discussions and perspectives on the structural and rheological characterisation of YSF for DIW.

Notes and references

1 R. Moreno, *J. Eur. Ceram. Soc.*, 2020, **40**, 559–587.
2 Y. Lakhdar, C. Tuck, J. Binner, A. Terry and R. Goodridge, *Prog. Mater. Sci.*, 2021, **116**, 100736.
3 W. Luo, Y. Wang, E. Hitz, Y. Lin, B. Yang and L. Hu, *Adv. Funct. Mater.*, 2017, **27**, 1701450.
4 S. Abdolhosseinzadeh, X. Jiang, H. Zhang, J. Qiu and C. J. Zhang, *Mater. Today*, 2021, **48**, 214–240.
5 A. Younis, C.-H. Lin, X. Guan, S. Shahrokhi, C.-Y. Huang, Y. Wang, T. He, S. Singh, L. Hu and J. R. D. Retamal, *et al.*, *Adv. Mater.*, 2021, **33**, 2005000.
6 B. Ling, R. Agrawal, D. He, R. J. Poole, A. I. Cooper, M. Liu and E. García-Tuñón, *Adv. Funct. Mater.*, 2024, 2405320.
7 G. V. Franks, C. Tallon, A. R. Studart, M. L. Sesso and S. Leo, *J. Am. Ceram. Soc.*, 2017, **100**, 458–490.
8 J. A. Lewis, *J. Am. Ceram. Soc.*, 2000, **83**, 2341–2359.
9 S. M. Shaban, J. Kang and D.-H. Kim, *Compos. Commun.*, 2020, **22**, 100537.
10 E. García-Tuñón, S. Barg, R. Bell, J. Weaver, C. Walter, L. Goyos and E. Saiz, *Angew. Chem.*, 2013, **52**, 7805.

11 A. Rajbanshi, E. Hilton, C. A. Dreiss, D. Murnane and M. T. Cook, *Macromol. Rapid Commun.*, 2024, **45**, 2300723.
12 M. Motornov, Y. Roiter, I. Tokarev and S. Minko, *Prog. Polym. Sci.*, 2010, **35**, 174–211.
13 P. Brown, C. P. Butts and J. Eastoe, *Soft Matter*, 2013, **9**, 2365–2374.
14 R. T. Woodward, L. Chen, D. J. Adams and J. V. Weaver, *J. Mater. Chem.*, 2010, **20**, 5228–5234.
15 R. T. Woodward and J. V. Weaver, *Polym. Chem.*, 2011, **2**, 403–410.
16 E. García-Tuñón, G. C. Machado, M. Schneider, S. Barg, R. V. Bell and E. Saiz, *J. Eur. Ceram. Soc.*, 2017, **37**, 199–211.
17 E. García-Tuñón, S. Barg, J. Franco, R. Bell, S. Eslava, E. D'Elia, R. C. Maher, F. Guitian and E. Saiz, *Adv. Mater.*, 2015, **27**, 1688–1693.
18 B. Bhat, S. Pahari, J. S.-I. Kwon and M. E. Akbulut, *Adv. Colloid Interface Sci.*, 2023, 103025.
19 R. H. Ewoldt and C. Saengow, *Annu. Rev. Fluid Mech.*, 2022, **54**, 413–441.
20 R. T. Woodward, R. A. Slater, S. Higgins, S. P. Rannard, A. I. Cooper, B. J. Royles, P. H. Findlay and J. V. Weaver, *Chem. Commun.*, 2009, 3554–3556.
21 M. Encheva, E. Muratspahic, C.-M. Saak, M. Zelenka, R. T. Woodward and E. H. Backus, *J. Colloid Interface Sci.*, 2025, **680**, 88–97.
22 E. García-Tuñón, R. Agrawal, B. Ling and D. J. Dennis, *Phys. Fluids*, 2023, **35**, 017113.
23 R. Agrawal and E. García-Tuñón, *Soft Matter*, 2024, **20**, 7429–7447.
24 K. Hyun, M. Wilhelm, C. O. Klein, K. S. Cho, J. G. Nam, K. H. Ahn, S. J. Lee, R. H. Ewoldt and G. H. McKinley, *Prog. Polym. Sci.*, 2011, **36**, 1697–1753.
25 R. H. Ewoldt, A. Hosoi and G. H. McKinley, *J. Rheol.*, 2008, **52**, 1427–1458.
26 M. Wilhelm, *Macromol. Mater. Eng.*, 2002, **287**, 83–105.
27 S. A. Rogers, B. M. Erwin, D. Vlassopoulos and M. Cloitre, *J. Rheol.*, 2011, **55**, 435–458.
28 C.-W. Lee and S. A. Rogers, *Korea-Aust. Rheol. J.*, 2017, **29**, 269–279.
29 S. A. Rogers and M. P. Lettinga, *J. Rheol.*, 2012, **56**, 1–25.
30 R. H. Ewoldt, P. Winter, J. Maxey and G. H. McKinley, *Rheol. Acta*, 2010, **49**, 191–212.
31 D. M. Hoyle, D. Auhl, O. Harlen, V. Barroso, M. Wilhelm and T. McLeish, *J. Rheol.*, 2014, **58**, 969–997.
32 A. Geffrault, H. Bessaies-Bey, N. Roussel and P. Coussot, *Addit. Manuf.*, 2023, **75**, 103752.
33 S. R. Cassin, S. Wright, S. Mckeating, O. B. Penrhyn-Lowe, S. Flynn, S. Lomas, P. Chambon and S. P. Rannard, *Polym. Chem.*, 2023, **14**, 1905–1914.
34 S. Flynn, S. D. Dale, A. B. Dwyer, P. Chambon and S. P. Rannard, *J. Polym. Sci., Part A: Polym. Chem.*, 2017, **55**, 3963–3967.
35 S. Flynn, A. B. Dwyer, P. Chambon and S. Rannard, *Polym. Chem.*, 2019, **10**, 5103–5115.
36 J. Rosselgong, S. P. Armes, W. R. Barton and D. Price, *Macromolecules*, 2010, **43**, 2145–2156.
37 W. Li, J. A. Yoon, M. Zhong and K. Matyjaszewski, *Macromolecules*, 2011, **44**, 3270–3275.
38 J. Rosselgong, S. P. Armes, W. Barton and D. Price, *Macromolecules*, 2009, **42**, 5919–5924.
39 P. J. Flory, *J. Am. Chem. Soc.*, 1941, **63**, 3083–3090.
40 P. J. Flory, *J. Am. Chem. Soc.*, 1941, **63**, 3091–3096.
41 S. R. Cassin, S. Flynn, P. Chambon and S. P. Rannard, *Polym. Chem.*, 2022, **13**, 2295–2306.
42 H. Cauldbeck, M. Le Hellaye, M. Long, S. M. Kennedy, R. L. Williams, V. R. Kearns and S. P. Rannard, *J. Controlled Release*, 2016, **244**, 41–51.
43 F. Isaure, P. A. Cormack and D. C. Sherrington, *J. Mater. Chem.*, 2003, **13**, 2701–2710.
44 C. Ferraro, E. García-Tuñón, S. Barg, M. Miranda, N. Ni, R. Bell and E. Saiz, *J. Eur. Ceram. Soc.*, 2018, **38**, 823–835.
45 A. Corker, H. C.-H. Ng, R. J. Poole and E. García-Tuñón, *Soft Matter*, 2019, **15**, 1444–1456.
46 Y. H. Shim and S. A. Rogers, *Phys. Fluids*, 2023, **35**, 063117.
47 J. Binner, A. McDermott, Y. Yin, R. M. Sambrook and B. Vaidhyanathan, *Ceram. Int.*, 2006, **32**, 29–35.
48 D. J. McClements and C. E. Gumus, *Adv. Colloid Interface Sci.*, 2016, **234**, 3–26.
49 J. S. Hong, H. J. Kong, K. Hyun, J. Bergfreund, P. Fischer and K. H. Ahn, *Rheol. Acta*, 2019, **58**, 453–466.
50 P. Wei, C. Cipriani, C.-M. Hsieh, K. Kamani, S. Rogers and E. Pentzer, *J. Appl. Phys.*, 2023, **134**, 100701.
51 R. J. Poole, *Rheol. Bull.*, 2012, **53**, 32–39.
52 R. Lenk and R. Lenk, *Polym. Rheol.*, 1978, 75–85.
53 K. M. Kamani and S. A. Rogers, *Proc. Natl. Acad. Sci. U. S. A.*, 2024, **121**, e2401409121.
54 R. Agrawal, E. García-Tuñón, R. J. Poole and C. P. Fonte, *J. Non-Newtonian Fluid Mech.*, 2025, 105407.
55 Q. Liu and W. Zhai, *ACS Appl. Mater. Interfaces*, 2022, **14**, 32196–32205.
56 S. S. Chan, M. L. Sesso and G. V. Franks, *J. Am. Ceram. Soc.*, 2020, **103**, 5554–5566.
57 C. O. Klein, H. W. Spiess, A. Calin, C. Balan and M. Wilhelm, *Macromolecules*, 2007, **40**, 4250–4259.
58 V. Hirschberg, M. Wilhelm and D. Rodrigue, *Polym. Test.*, 2017, **60**, 343–350.
59 X. Zhao, D. Li, L.-J. Wang and Y. Wang, *Carbohydr. Polym.*, 2022, **281**, 119061.
60 X. Zhao, D. Li, L.-J. Wang and Y. Wang, *Food Hydrocolloids*, 2023, **135**, 108208.
61 S. Migliozzi, Y. He, M. Parhizkar, Y. Lan and P. Angeli, *Soft Matter*, 2024, **20**, 8621–8637.
62 A. J. Sandoval, M. Fernández, O. Sanz, A. Santamara, E. Penott-Chang and A. J. Müller, *J. Rheol.*, 2022, **66**, 859–879.
63 C. Saengow, S. Sen, J. Yus, E. E. Lovrich, A. G. Hoika, K. M. Chang, A. A. Pfeil, N. Haug, A. J. W. Johnson and R. H. Ewoldt, *arXiv*, 2025, preprint, arXiv:2501.12630, DOI: **10.48550/arXiv.2501.12630**.

